Check for updates

JGR Solid Earth

RESEARCH ARTICLE
10.1029/2022JB024484

Optimizing a Model of Coseismic Rupture for the 22 July 2020 M_W 7.8 Simeonof Earthquake by Exploiting Acute Sensitivity of Tsunami Excitation Across the Shelf Break

Yefei Bai[1,2], Chengli Liu[3], Thorne Lay[4], Kwok Fai Cheung[5], and Lingling Ye[6]

[1]Ocean College, Zhejiang University, Zhoushan, China, [2]Hainan Institute, Zhejiang University, Sanya, China, [3]Institute of Geophysics and Geomatics, China University of Geosciences, Wuhan, China, [4]Department of Earth and Planetary Sciences, University of California Santa Cruz, Santa Cruz, CA, USA, [5]Department of Ocean and Resources Engineering, University of Hawaii at Manoa, Honolulu, HI, USA, [6]Department of Earth and Space Sciences, Southern University of Science and Technology, Shenzhen, China

Key Points:

- Published finite-fault models for the 2020 M_W 7.8 earthquake predict varying tsunami signals despite having similar slip patterns
- The tsunami excitation is very sensitive to the absolute placement of slip relative to the shelf break and along strike
- Iteration of slip inversion parameters and tsunami predictions optimizes the model to fit all data well with slip only beneath the shelf

Supporting Information:

Supporting Information may be found in the online version of this article.

Correspondence to:

Y. Bai,
yfbai@zju.edu.cn

Citation:

Bai, Y., Liu, C., Lay, T., Cheung, K. F., & Ye, L. (2022). Optimizing a model of coseismic rupture for the 22 July 2020 M_W 7.8 Simeonof earthquake by exploiting acute sensitivity of tsunami excitation across the shelf break. *Journal of Geophysical Research: Solid Earth*, *127*, e2022JB024484. https://doi.org/10.1029/2022JB024484

Received 29 MAR 2022
Accepted 15 JUN 2022

© 2022. The Authors.
This is an open access article under the terms of the Creative Commons Attribution-NonCommercial-NoDerivs License, which permits use and distribution in any medium, provided the original work is properly cited, the use is non-commercial and no modifications or adaptations are made.

Abstract The Shumagin seismic gap along the Alaska Peninsula experienced a major, M_W 7.8, interplate thrust earthquake on 22 July 2020. Several available finite-fault inversions indicate patchy slip of up to 4 m at 8–48 km depth. There are differences among the models in peak slip and absolute placement of slip on the plate boundary, resulting from differences in data distributions, model parameterizations, and inversion algorithms. Two representative slip models obtained from inversions of large seismic and geodetic data sets produce very different tsunami predictions at tide gauges and deep-water pressure sensors (DART stations), despite having only secondary differences in slip distribution. This is found to be the result of the acute sensitivity of the tsunami excitation for rupture below the continental shelf in proximity to an abrupt shelf break. Iteratively perturbing seismic and geodetic inversions by constraining fault model extent along dip and strike, we obtain an optimal rupture model compatible with teleseismic *P* and *SH* waves, regional three-component broadband and strong-motion seismic recordings, hr-GNSS time series and static offsets, as well as tsunami recordings at DART stations and regional and remote tide gauges. Slip is tightly bounded between 25 and 40 km depth, the up-dip limit of slip in the earthquake is resolved to be well-inland of the shelf break, and the rupture extent along strike is well-constrained. The coseismic slip increased Coulomb stress on the shallow plate boundary extending to the trench, but the frictional behavior of the megathrust below the continental slope remains uncertain.

Plain Language Summary Several studies on the 22 July 2020 M_W 7.8 thrust event have included finite-fault inversions, yielding generally consistent slip models. However, none of these studies have fully considered the seismic and geodetic data together with the tsunami measurements at tide gauges and deep-water pressure sensors. We select two representative slip models obtained from prior seismic and geodetic inversions for tsunami modeling and find that they give distinct tsunami predictions despite having only a minor shift of slip by ∼20 km relative to shelf break. Large differences in tsunami excitation occur when seafloor deformation extends to the continental slope under deeper water. We perform iterative inversion of seismic and geodetic observations and forward modeling of tsunami signals to obtain an optimal slip model compatible with teleseismic waves, regional seismic recordings, hr-GNSS time series and static offsets, along with tsunami recordings at DARTs and tide gauges. Precise placement of the slip distribution beneath the continental shelf controls the strength and timing of seaward tsunamis, with waveforms varying nonlinearly with seafloor deformation extending across the shelf break. The earthquake increased Coulomb stress on the shallow megathrust, but uncertainty in the shallow frictional behavior leaves it unclear whether a future large event can occur there.

1. Introduction

The boundary between the underthrusting Pacific plate and the North American plate beneath western Alaska generates great earthquakes along most of its length, with an important exception being a ∼300 km segment along the trench near the Shumagin Islands, between the rupture zones of the 1938 (M_W 8.2) and 1946 (M_W 8.6) earthquakes (Figure 1a). This segment along the Alaska Peninsula was designated as the Shumagin seismic gap (e.g., Boyd & Lerner-Lam, 1988; Boyd et al., 1988; Davies et al., 1981; Sykes et al., 1981), with dimensions that

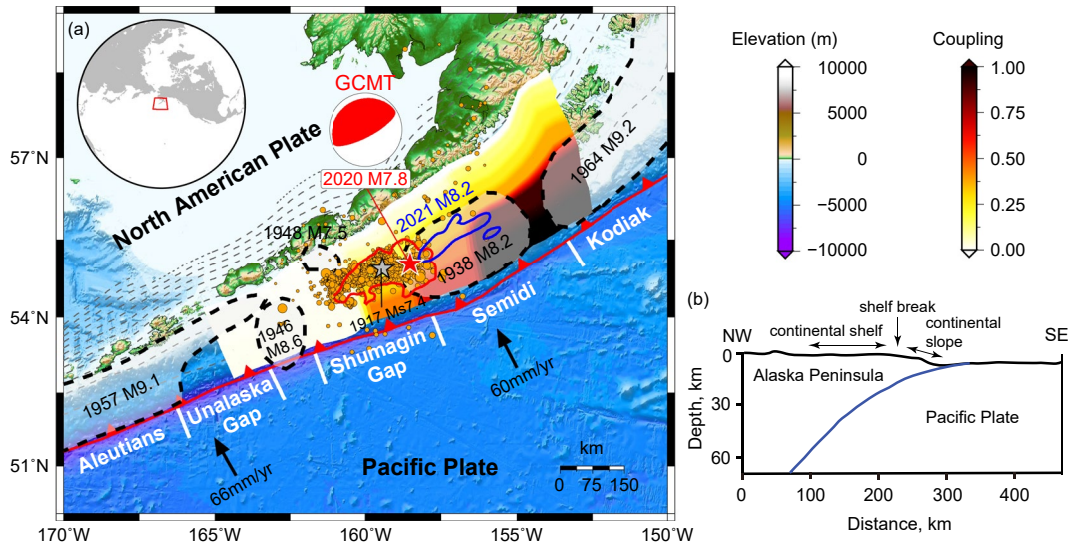

Figure 1. (a) Regional base map showing the Aleutians-Alaska subduction zone with rupture zones for the 1938, 1946, 1957, 1964, 2020, and 2021 earthquakes. The Pacific plate underthrusts the North American plate along the Aleutian-Alaska subduction zone. The relative velocity and direction of motion of the Pacific plate, holding North America fixed, is indicated by black arrows (DeMets et al., 2010). Dark black dashed regions indicate the aftershock zones of great earthquakes in 1957, 1946, 1938, and 1964 associated with the segments along the subduction zone from the Aleutians to the Kodiak Island region. The early aftershocks (gold circles) and the hypocenter (red star), with the global centroid moment-tensor (GCMT) focal mechanism and the 0.5 m slip contour for the finite-fault model of Liu et al. (2020) highlight the 2020 *Mw* 7.8 Simeonof earthquake, which ruptured within the Shumagin seismic gap. The blue contour outlines the 2 m slip contour for the 2021 Chignik earthquake in the adjacent Semidi segment (Ye et al., 2022). The hypocentral location of the 1917 *Ms* 7.4 rupture within the 2020 rupture zone is indicated by the gray star. Light dashed contours indicate 20 km depth increments along the Slab2 plate interface model (Hayes et al., 2018). The yellow to black color pallette indicates the estimated plate coupling inferred from geodetic observations by Li and Freymueller (2018). (b) Schematic NW-SE cross-section through the arc near the 2020 rupture zone, indicating the broad flat continental shelf overlying the rupture zone, the shelf break, and the continental slope.

can accommodate an event as large as M_W 8.3. On July 22, 2020, an M_W 7.8 earthquake ruptured the down-dip eastern portion of the Shumagin gap, with the hypocenter [06:12:44.8 UTC; 55.072°N, 158.596°W, 28.0 km depth; U.S. Geological Survey National Earthquake Information Center (USGS-NEIC), https://earthquake.usgs.gov/earthquakes/eventpage/us7000asvb/executive] being located near the eastern end of a ~225 km long by ~100 km wide early aftershock zone (Figure 1a). A routine finite-fault slip inversion of teleseismic body and surface waves by the USGS-NEIC (https://earthquake.usgs.gov/earthquakes/eventpage/us7000asvb/finite-fault) gives a very patchy slip distribution over the depth range of 8–48 km, with peak slip of 4 m near the hypocenter and significant slip extending beyond the continental shelf break (Figure 1b) at a water depth of 200 m. This event, designated the Simeonof earthquake, was larger than a previous M_W ~ 7.4 earthquake in 1917 (Estabrook & Boyd, 1992) which it appears to have overlapped (Ye et al., 2021). There is no evidence of tsunami deposits from prior great earthquakes or of strong vertical motions on Simeonof Island over the past 10,000 years (e.g., Briggs et al., 2014; U.S.G.S., 2013; Witter et al., 2014).

Geodetic investigations show that the plate boundary along the eastern Shumagin gap region had been accumulating only modest strain overall during preceding decades (e.g., Drooff & Freymueller, 2021; S. Li & Freymueller, 2018), and the western region appears to have essentially no strain accumulation (Freymueller & Beavan, 1999). However, there is very limited resolution of any slip deficit in the shallow portion of the zone. Thus, the question arises as to whether the 2020 event represents the largest earthquake that might occur in the Shumagin segment, or whether a large slip deficit may still be accumulating seaward of the 2020 rupture zone that could produce a rupture comparable to the great near-trench 1946 tsunamigenic earthquake in the adjacent arc segment to the southwest (Figure 1a) where no geodetic slip deficit is detected in the island arc, although as noted above there is no evidence that such events have occurred. The devastating local and far-field tsunami impacts for the 1946 event, particularly at Scotch Cap on Unimak Island and in Hawaii, add urgency to resolving this issue. Establishing robust constraints on the coseismic slip distribution for the 2020 event, particularly its

up-dip slip extent and occurrence of any shallow afterslip, along with evaluating the general nature of tsunami excitation process in the Shumagin region with an unusual broad shallow continental shelf (Figure 1b), are central to assessing the potential for additional large megathrust or splay faulting earthquakes in the unruptured portions of the seismic gap to produce damaging tsunamis.

The importance of the 2020 Simeonof earthquake has prompted several seismo-geodetic analyses of the faulting process, aftershock sequence and afterslip, primarily motivated to constrain the location and configuration of the coseismic slip and its relationship to prior estimates of slip deficit in the region. A multi-time window kinematic slip inversion of three-component 1-Hz GNSS displacements from seven stations and three-component filtered ground-velocities from six accelerometers by Crowell and Melgar (2020) gives a slip model very different from the USGS solution, with large-slip of up to 2 m concentrated beneath the Shumagin Islands and little slip at or up-dip of the hypocenter. A second model, obtained by inversion of teleseismic *P* and *SH* displacements, three-component broadband and strong-motion ground velocities, and GNSS static offsets by Liu et al. (2020), has three predominant slip patches, with up to 1.6 m of slip near the hypocenter, up to 3.2 m of slip beneath the Shumagin Islands, and up to 1.5 m of slip in a western patch which was not detected by Crowell and Melgar (2020). A linear least-squares multi-time window kinematic inversion of teleseismic *P* and *SH* ground motions and coseismic static offsets by Ye et al. (2021) produced a slip model with ∼2 m slip near the hypocenter, a slip patch of up to 4 m beneath the Shumagin Islands, and a slip patch of up to ∼1 m further to the west with an overall rupture velocity of ∼3 km/s. The primary slip patch under the Shumagin Islands is about the same dimension and has about the same location in the latter two models. A fourth model inverted static GNSS displacements, high-rate GNSS waveforms, teleseismic waveforms, and InSAR displacements (Xiao et al., 2021). This inversion inferred an average rupture velocity of 1.9 km/s with a peak slip of 2.2 m beneath the eastern Shumagin Islands, and is quite similar in spatial distribution of slip to the model of Liu et al. (2020). These finite-fault models all adjusted their model geometry to conform to the general orientation of the slab interface model Slab2 (Hayes et al., 2018), but they differ in subfault discretization (rectangular vs. triangular subfaults), data distribution, and details of the inversions. This is typical of the status of studies for any large earthquake, and in this case, all four models exploit the unusual availability of geodetic observations directly above the rupture zone, and provide a relatively consistent first-order characterization of the rupture, with resolved slip located in the depth range of 20–45 km along the megathrust where early aftershocks are concentrated (Figure 1a).

Given that there are general similarities, but also some differences in the seismo-geodetic rupture models for the 2020 event, and given the importance of resolving the along-dip coseismic slip distribution with as much confidence as possible, the 2020 earthquake slip model can be further constrained by recordings of tsunami signals at regional and far-field tide gauges and in deep-water seafloor pressure gauges of the NOAA DART network. Mulia et al. (2022) utilized the static GNSS displacement along with tsunami observations in a linear waveform inversion to provide a slip distribution comparable to those of Liu et al. (2020), Ye et al. (2021), and Xiao et al. (2021). The 2020 Simeonof earthquake was only weakly tsunamigenic, producing very long-period tsunami signals, as noted by Ye et al. (2021) and Mulia et al. (2022), with recorded tsunami amplitudes being at most ∼30 cm locally in the Shumagin Islands (e.g., Larson et al., 2021) and less than 1 cm in deep water of the north Pacific (e.g., Ye et al., 2021). However, the very slow propagation of tsunami waves provides enhanced sensitivity to the absolute location of seafloor motion produced by underlying faulting. In this case of rupture below a shallow, relatively flat continental shelf at water depths less than 200 m (Figure 1b), the tsunami complexity arising from direct wave excitation and shelf reverberation (e.g., Ye et al., 2016) adds sensitive resolution to coseismic slip placement, particularly with respect to the shelf break where tsunami propagation speed increases and wave period decreases correspondingly as the water deepens rapidly. The sensitivity of the wave period can be complicated by tsunami generation across the shelf break and nonlinear wave interactions in the shallow shelf environment, especially around the Shumagin Islands, where the rupture is directly below. We improve accuracy and confidence in the 2020 slip distribution by iteratively inverting a comprehensive seismic and geodetic data set and predicting the tsunami recordings generated by the kinematic seafloor deformation with a nonhydrostatic wave model in forward computation that accounts for nonlinear wave interactions. We adjust the fault model parameters until convergence on a satisfactory model that fits all of the considered data well. The final model provides a representation of the coseismic faulting with high confidence for pursuing the outstanding issues of up-dip coseismic rupture extent, afterslip, and extent of any shallow slip deficit accumulation.

2. Representative Finite-Fault Slip Models for the 2020 Simeonof Earthquake

We evaluate the tsunami predictions for two representative finite-fault models for the 2020 M_W 7.8 Simeonof earthquake (Liu et al., 2020; Ye et al., 2021) obtained by independent inversions of large data sets of global teleseismic *P* and *SH* recordings from the Incorporated Research Institutions for Seismology (IRIS), and regional GNSS coseismic static displacements from UNAVCO and the University of Nevada Reno. The model of Liu et al. (2020) also inverted regional broadband and strong-motion three-component signals. Figure 2 depicts the slip distributions from these two planar fault models in map position, along with predicted seafloor uplift and subsidence calculated for each model following Okada (1985). Liu et al. (2020) used a fault geometry with strike, $\phi = 245°$ and dip, $\delta = 16°$ and a hypocenter 28 km deep, while Ye et al. (2021) used $\phi = 245.9°$, $\delta = 18.9°$, and a hypocenter 23 km deep. Three patches of large slip are apparent in each model, with the largest central patch located beneath the Shumagin Islands. The model of Liu et al. (2020) (Figure 2b) has somewhat more distributed slip, which spreads the seafloor uplift region further along strike and further toward the trench than for the model of Ye et al. (2021). The model of Mulia et al. (2022) produces seafloor deformation intermediate between these two models, while the finite-fault model of Xiao et al. (2021) produces a similar extent of seafloor deformation to the model of Liu et al. (2020).

The two finite-fault models in Figure 2 fit their data sets very well respectively, and the subtle differences in the slip patterns are typical of those among finite-fault models obtained for any given large event (e.g., Lay, 2018). It is well known that finite-fault models are non-unique, and usually this level of difference is attributed to the limited resolution of the geophysical inverse problem and differences in data sets and weighting, prescribed fault model geometry and kinematic parameters, and inversion procedures. The most systematic difference in this case is that the model of Liu et al. (2020) has a slip distribution shifted about 20 km closer to the trench than the model of Ye et al. (2021). This results in some seafloor uplift occurring beyond the shelf break, which is near the 200 m depth contour. This difference is important for the issue of the up-dip limit of coseismic slip and the potential for any seaward portion of the megathrust to generate a large tsunami earthquake, so we turn to an additional, complementary data set of tsunami observations that can improve absolute placement of slip on the plate boundary.

3. Tsunami Recording Predictions

The seafloor deformation and timing for a given model in Figure 2 is used to compute the near-field and far-field tsunamis over available bathymetry using the non-hydrostatic model NEOWAVE (Yamazaki, Cheung, et al., 2011; Yamazaki et al., 2009). This staggered finite difference code uses the nonlinear shallow-water equations with a vertical velocity term that can describe tsunami generation from kinematic seafloor deformation as well as flows on steep slopes and dispersion across the ocean for computation of DART and tide gauge signals (Bai et al., 2015). The method of Tanioka and Satake (1996) is applied to account for vertical seafloor motion from horizontal displacement of slopes, which is important beyond the shelf break. Modeling of tsunami processes from the open ocean to the shore requires a system of two-way nested computational grids. Figure 3a shows the coverage of the level-1 grid extending from Alaska to Hawaii and California with 2-arcmin resolution for optimal model dispersion properties (L. Li & Cheung, 2019). The level-2 grids around the source region and the Hawaiian Islands provide transitions to the level-3 grids (Figure 3b1–b3), which resolve shelf hydraulic processes at 6 arcsec along the Alaska Peninsula and near Maui and Hawaii Islands. Figure 3c1–c3 shows level-4 grids at 0.3 arcsec for computation of the tsunami signals at the Sand Point, Kahului, and Hilo tide gauges. The subgrid roughness, which becomes a factor in shelf hydraulic processes, is described by a Manning's number of 0.025. The 0.5-arcmin GEBCO dataset provides the background digital elevation model, which is augmented by high-resolution NCEI datasets for the Alaska Peninsula as well as LiDAR and multibeam data of 1–50 m resolution in Hawaii waters.

The computed sea surface elevations at the DART stations (Figure 3a shows their locations) are compared with the observations in Figure 4 for the finite-fault rupture models of Ye et al. (2021) and Liu et al. (2020). The de-tided, low-pass filtered (retaining periods less than 7,200 s) time series are shown along with the corresponding spectra. High-frequency seismically-induced motions are apparent at all stations, and these overwhelm the first tsunami wave arrival at DARTs 46403 and 46410, but later long-period sea surface variations are observed at these stations, despite some unexpected pulses between hours 2 and 5 in DART 46410. The NEOWAVE

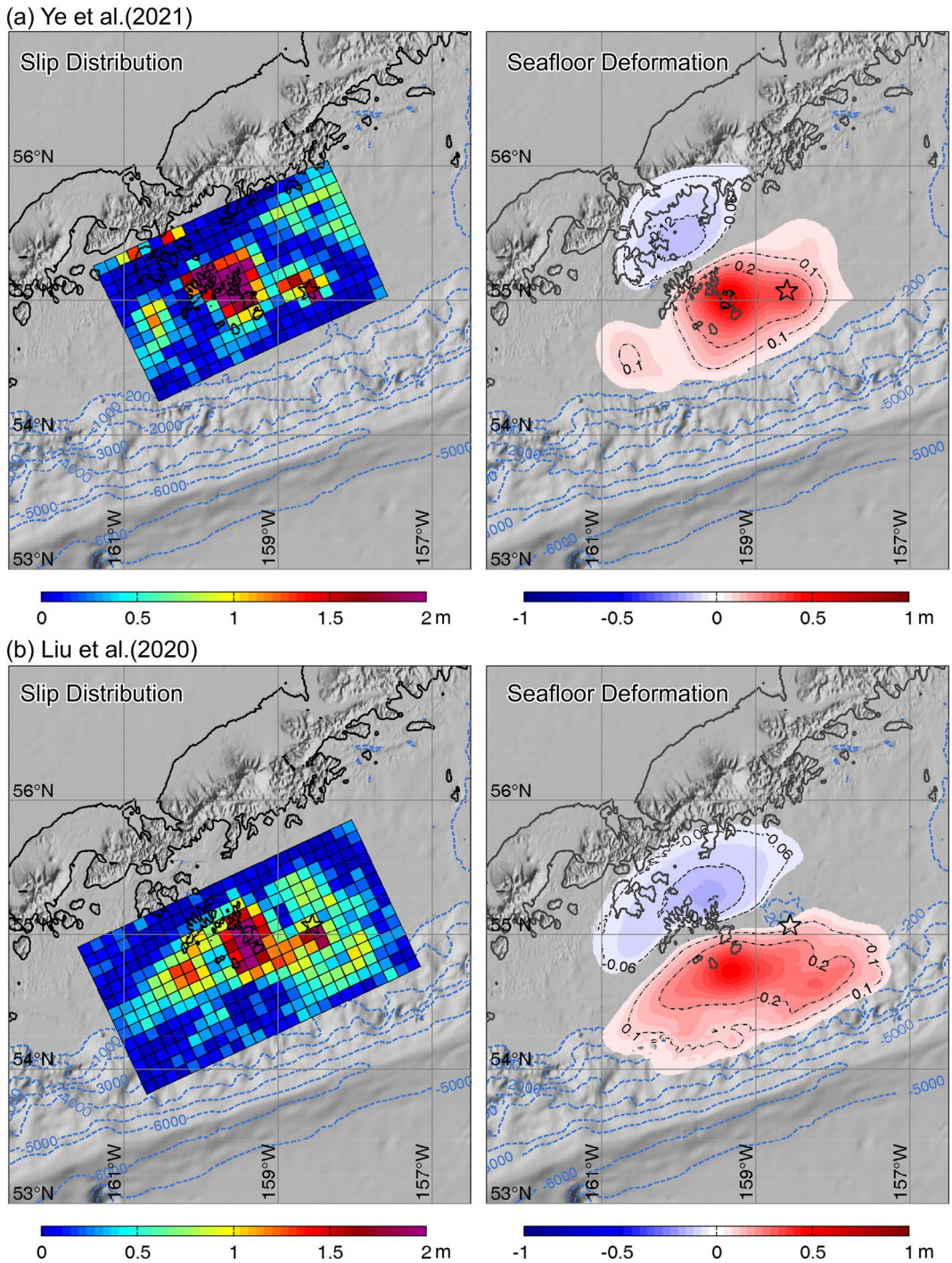

Figure 2. Maps of the published slip models for the 2020 Simeonof earthquake from (a) Ye et al. (2021) and (b) Liu et al. (2020) showing slip distributions and seafloor subsidence and uplift distributions. The black open star denotes the epicenter. The light dashed blue contours indicate water depth in meters. The 200 m contour corresponds to the continental shelf break, with the continental slope extending seaward to the trench.

predictions do not account for the seismic motions, and show long-period arrivals with sea surface elevations of <1 cm for all stations. The low amplitudes were noted and corresponding calculations for the finite-fault model were shown by Ye et al. (2021), which gave acceptable predictions of most first tsunami arrivals and overall low amplitude despite the limited match to the waveforms (Figure 4a). Liu et al. (2020) did not model the tsunami

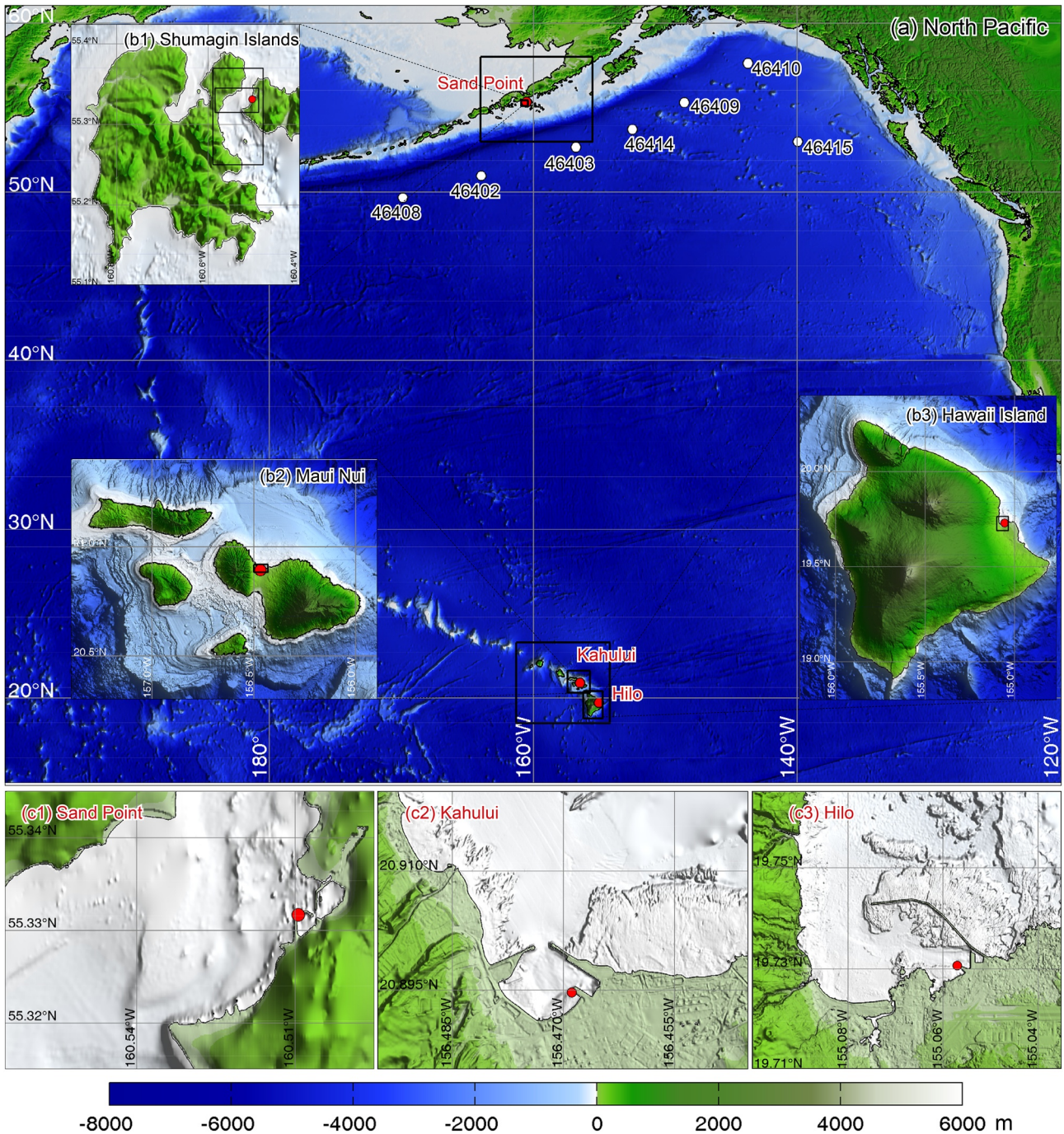

Figure 3. Computational grid system, bathymetry, and location maps. (a) Level 1 with outlines of nested level-2 and -3 grids indicated by black rectangles, DART locations by white circles, and Sand Point and Hawaii tide gauges by red circles. (b) Level 3 for Shumagin Islands (b1) with outlines of nested level-4 and level-5 grids, Maui Nui (b2) with outline of level-4 grid, and Hawaii Island (b3) with outline of level-4 grid. (c) Level-4 bathymetry maps for Sand Point (c1), Kahului (c2), and Hilo (c3).

signals, and in general, our calculations indicate that the first tsunami arrivals are overpredicted in amplitude and too early for DARTS 46408, 46402, 46414, 46409, and 46415, but the later reverberations are more accurately matched (Figure 4b).

The tide gauge predictions for the two models are shown in Figure 5. Comparable fits are found at regional station Sand Point for both models with observed amplitudes no larger than 50 cm. However, there are very

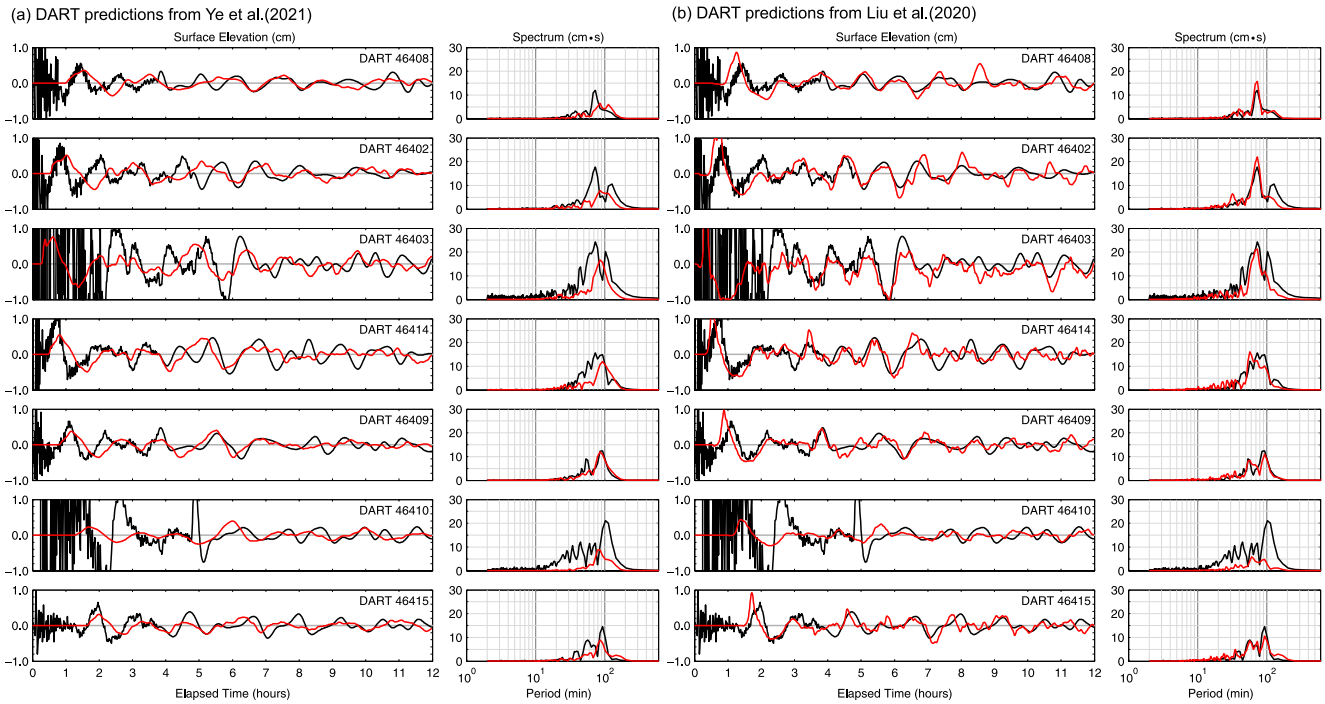

Figure 4. Tsunami predictions at DARTs for the finite-fault slip models of (a) Ye et al. (2021) and (b) Liu et al. (2020). Observed, de-tided, and lightly low-pass filtered sea surface elevations inferred from sea-floor pressure records are shown in black; predicted tsunami signals are shown in red. The time series (left column in each part) include high frequency signals generated by passage of seismic waves; these are not included in the model calculations for the tsunami. Amplitude spectra are shown in the right column of each part.

large amplitude differences between the model predictions at the Hilo and Kahului tide gauges in Hawaii. The observed signal amplitudes are very low, <10 cm, close to the noise level, and interference with local background oscillations of several centimeters generated by large swell and wind waves near Hawaii is expected (e.g., Azouri, 2016). This can modify the tsunami signals with destructive or constructive interference, making it difficult to confidently identify the arrival times and amplitudes of the weak tsunami signal. The tsunami predictions for the model of Ye et al. (2021) are very low, below the observed levels, which could suggest that the local noise dominates the signals. In contrast, the tsunami predictions for the model of Liu et al. (2020) are much larger than the observed signals, and the local noise level is not expected to greatly interfere with such large signals. Even with the prediction of the seaward DART stations being larger for this model, it is striking that the two similar faulting representations produce such different predictions in the far-field tsunami.

Maps of predicted peak sea surface elevation across the northern Pacific for the two models are shown in Figure 6. While landward tsunami amplitudes are similar due to comparable seafloor deformation and energy trapping within the continental shelf, accounting for the similarity of the predictions at Sand Point, much higher amplitudes are predicted seaward of the Liu et al. (2020) rupture model, extending all the way to Hawaii and California. This remarkable difference in tsunami amplitudes is a direct consequence of the ~20 km seaward shift of the megathrust slip distribution in the model of Liu et al. (2020) relative to Ye et al. (2021) shown in Figure 2. The models have modest differences in peak slip and slip distribution as well. While the larger areal extent of the seafloor uplift produced by Liu et al. (2020) plays a role in enhancing longer period tsunami waves, most of the energy is trapped on the shelf with gradual leakage of waves that are further reduced in amplitude by deshoaling on the continental slope. The primary effect causing the differences in Figure 6 is having uplift extend seaward of the shelf break, exciting shorter period tsunami waves that directly propagate seaward over increasing water depth with less deshoaling. This produces the strong lobe of seaward-directed tsunami radiation that enhances the signals predicted at Hawaii tide gauges.

The comparisons of predicted tsunami signals for the rupture models of Liu et al. (2020) and Ye et al. (2021) suggest that the precise placement of slip on the fault relative to the shelf break has very strong effects on seaward tsunami radiation. This is clearly demonstrated in the computed DART signals for a series of simple uniform slip

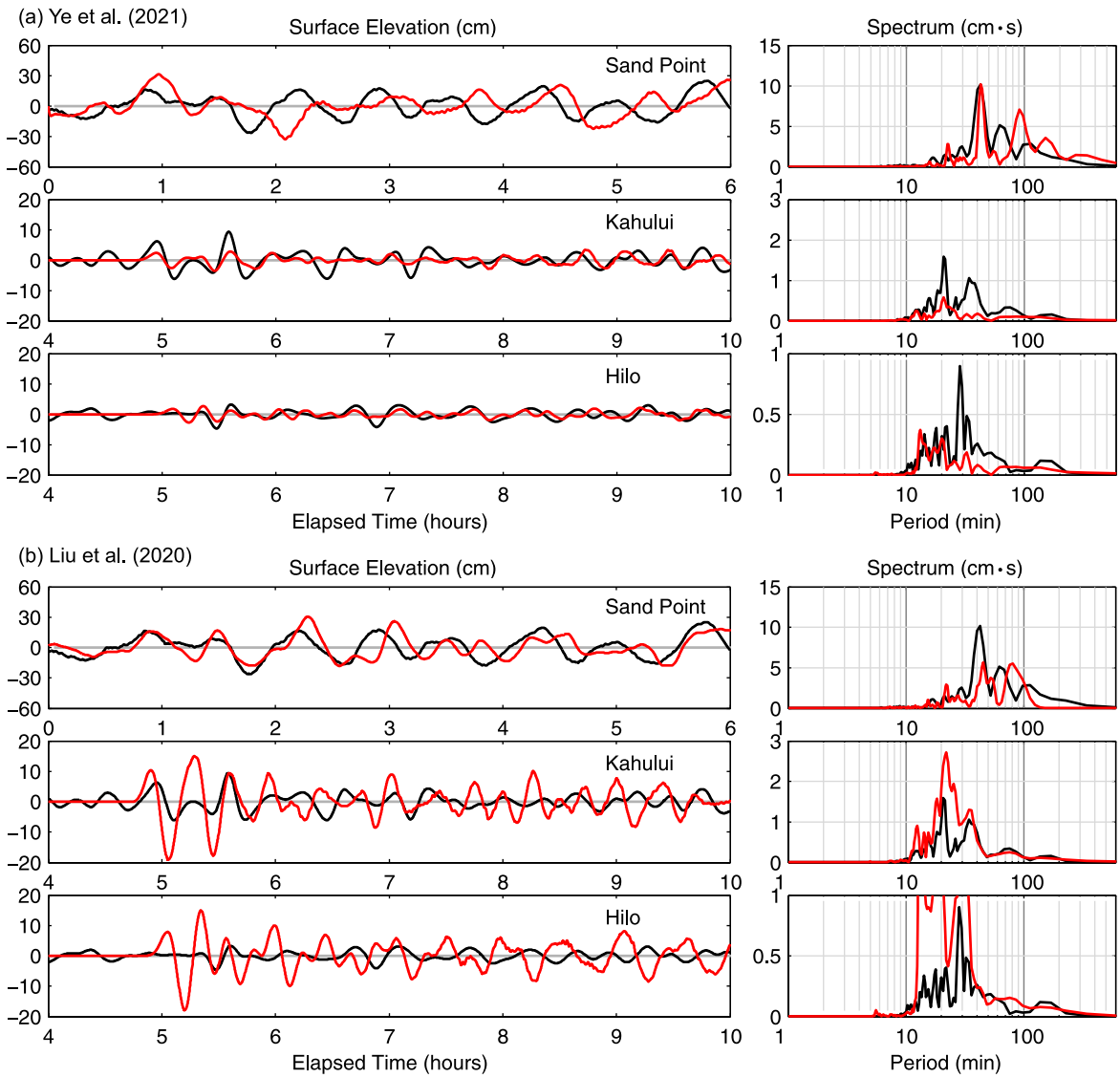

Figure 5. Tsunami observations and predictions at regional (Sand Point) and Hawaii (Hilo, Kahului) tide gauges for finite-fault models of (a) Ye et al. (2021) and (b) Liu et al. (2020). Observed time series (left) and amplitude spectra (right) are shown with black lines and model predictions are shown with red lines.

models in Figure S1 in Supporting Information S1. While the radiated wave amplitude increases and the travel time shortens with offshore shift of the slip model, the tsunami wave period is inversely proportional to the square root of the water depth near the source region. The model of Liu et al. (2020) overpredicts the first arrival amplitudes and produces too early arrival times at the DART stations, and greatly overpredicts the Hawaii tide gauge signals, indicating excess uplift beyond the shelf break. The extensive sequence of later arrivals at the DART stations from the leaked shelf oscillations is relatively well predicted by that model. The model of Ye et al. (2021) somewhat underpredicts the amplitudes of first arrivals at DART stations and overpredicts their period due to the majority of the excitation being on the shelf, and the model does not predict the later arrivals very well. It produces very weak signals at the Hawaii tide gauges. While each model satisfactorily predicts the seismic and geodetic data that were used in their derivation, the relatively poor fit to tsunami signals compared to that typically achieved for seismic, geodetic, and tsunami data sets in prior studies of large events (e.g., Yamazaki, Lay, et al., 2011) indicates that additional constraints may be placed on the 2020 Simeonof rupture model by including tsunami data in the modeling.

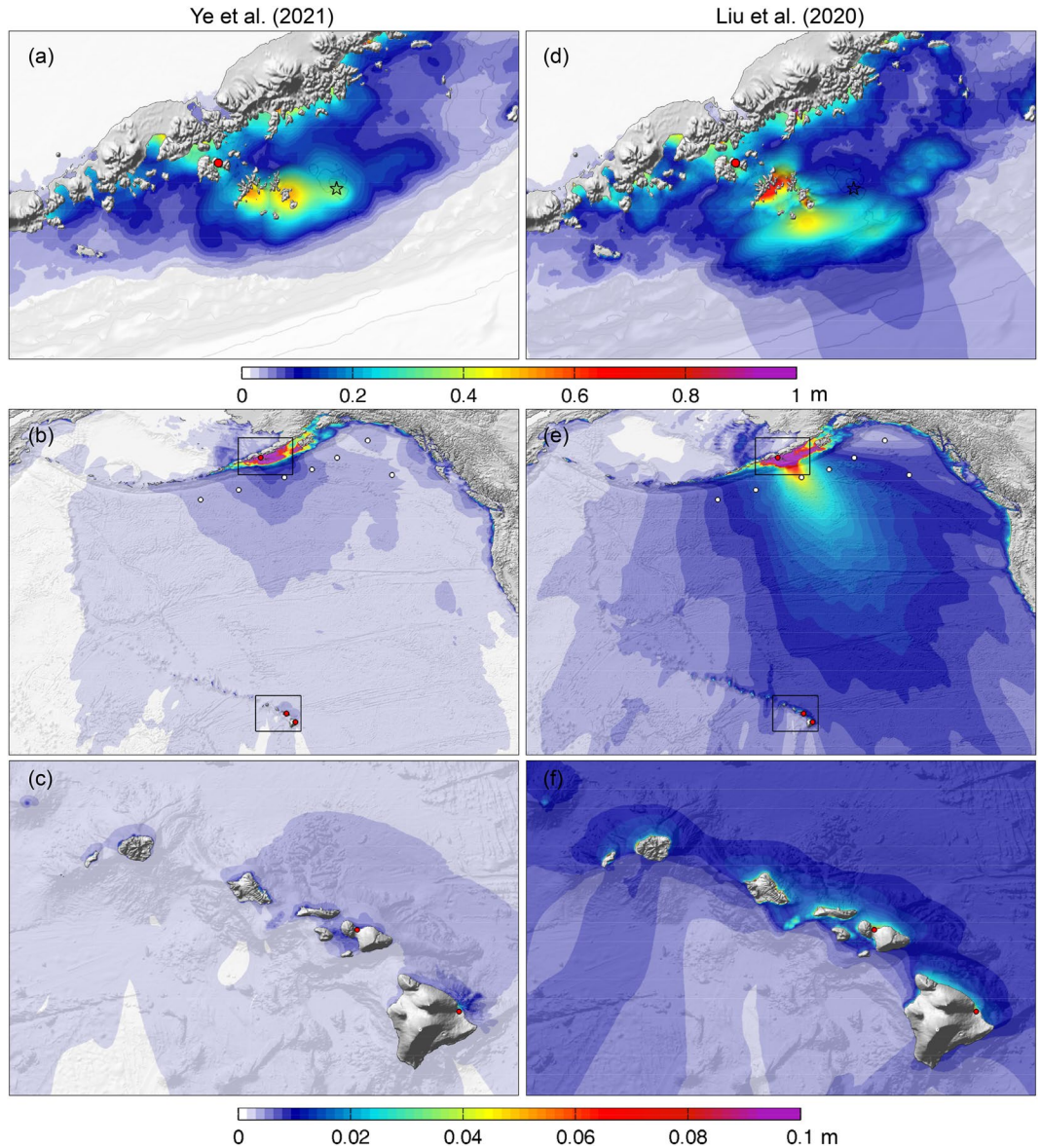

Figure 6. Maximum sea surface elevation maps extending from the source region across the northern Pacific to Hawaii predicted for the finite-source models of (a–c) Ye et al. (2021) and (d–f) Liu et al. (2020). (a and d) Along the Aleutians. (b and e) Across the Pacific. (c and f) Around Hawaii. The black open star denotes the epicenter. Red circles indicate the tide gauges and white circles denote the DART stations.

4. Optimized Model From Iterative Inversion

The acute sensitivity of tsunami excitation to the placement of the megathrust slip distribution for a large event evident in the preceding model comparisons is a consequence of the shallow ocean overlying the very flat continental shelf offshore of the Alaska Peninsula, adjacent to the steep continental slope that extends to the Aleutian trench (Figure 1b). We pursue an iterative modeling procedure, beginning with the model of Liu et al. (2020), to seek a model consistent with the full set of seismic, geodetic, and tsunami observations for the 2020 Simeonof earthquake. The strategy of the iterative procedure is to perform inversions for a finite-fault model representation using the seismic and geodetic data sets, predict the tsunami signals at tide gauge and DART stations through forward modeling, and then perturb the fault model geometry as needed to improve the fits. This type of procedures has been successfully used to achieve self-consistent faulting representations using multiple data sets for many events, most of which have large slip beneath continental slopes (e.g., Bai et al., 2014; Heidarzadeh et al., 2016;

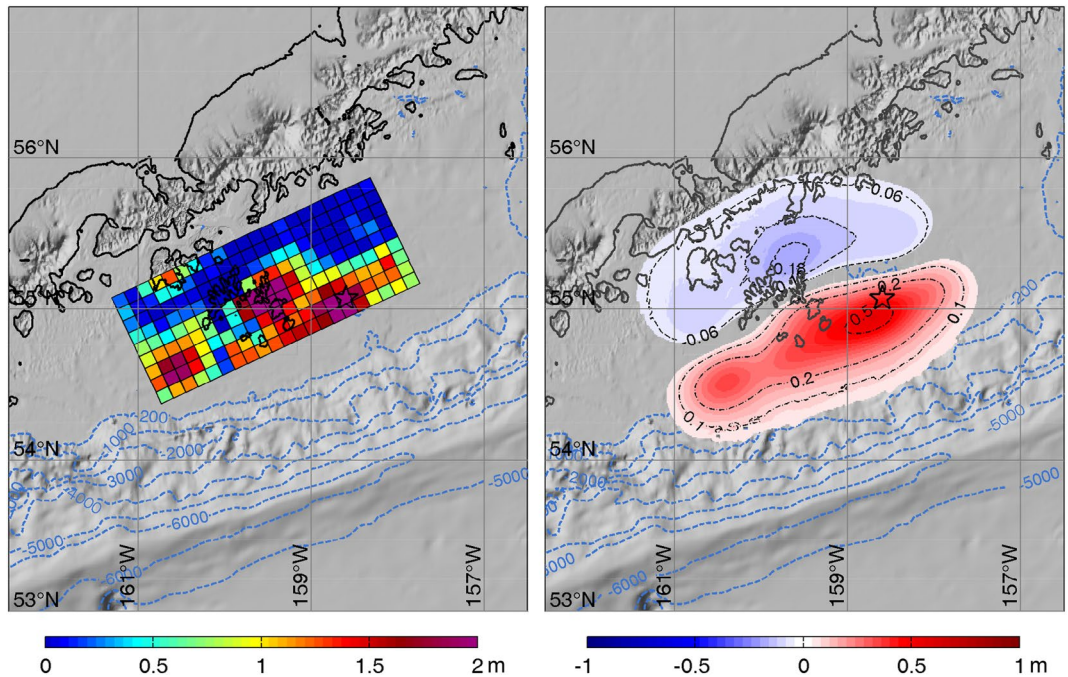

Figure 7. Map of the final finite-fault model from iterative inversion and forward modeling showing coseismic slip distribution (left) and seafloor subsidence and uplift distribution (right). The black open star denotes the epicenter. The light dashed blue contours indicate water depth in meters.

L. Li et al., 2016; Yamazaki et al., 2013; Yamazaki, Lay, et al., 2011; Ye et al., 2016; Yue et al., 2014). Given that perturbation of the model dimensions and geometry involves nonlinear feedback of the predictions for all data, particularly with the strong sensitivity of the tsunami waves, we do not perform joint inversions including the tsunami data, but still converge quickly on successful model parameters.

We include hr-GPS time series data that were not originally available for the analysis by Liu et al. (2020) in the seismo-geodetic inversion, enhancing the geodetic information by the explicit travel time information in the hr-GPS ground displacements at close distances. The inversion procedure is the same as that used in Liu et al. (2020), based on the method of Ji et al. (2002, 2003), with the source velocity structure and kinematic parameters of the rupture being the same as in the prior modeling. The strike and dip of the starting model were also kept fixed. The primary model perturbations performed involved removal of rows from the model at shallow depth and along strike relative to the starting model in Figure 2b. As there was only minor slip toward the edges of the original model (generally viewed as a desirable feature of finite-fault inversions), several rows and columns on either end of the fault model could be removed with no impact on inversion of the seismic and geodetic data. Nonetheless, removal of shallow model rows with low slip directly reduced modeled tsunami amplitudes at the DART stations and Hawaii tide gauges and delayed the initial arrival times, both of which improved fit to the seaward tsunami observations. With steady improvement of the tsunami predictions, the number of rows along dip was reduced from 14 to 9, and the number of columns along strike was reduced from 25 to 21, with the hypocenter of the final model [updated from that used by Liu et al. (2020) for a revised location by the USGS to 55.07°N, 158.60°W] being located in the second row down-dip and the sixth column along strike from the northeastern end.

The final model is shown in Figure 7, with the three large-slip-patch character indicated in Figure 2 still being evident, but more uniform slip along strike and rather abrupt slip truncation along the seaward edge resulting from the constrained up-dip extent of the rupture. However, this is a required outcome to achieve good prediction of the seaward tsunami arrival times and amplitudes. The down-dip edge of slip is well-resolved and pronounced along the rupture with only a small, poorly resolved slip patch being located deeper on the plate interface. The corresponding surface deformation (Figure 7) is narrower along dip with uplift peaking at ~0.5 m slightly seaward of the hypocenter and reaching ~0.1 m beyond the shelf edge at 200 m depth. Small northwestward perturbations

of the hypocenter by up to 10 km were explored, but did not improve tsunami fits and gave minor degredation of the fits to regional seismic stations.

The model in Figure 7 produces very good synthetic predictions of the large broadband teleseismic *P* and *SH* wave ground velocity data set (Figure 8), the regional three-component broadband and strong motion ground velocities (Figure 9a) and the hr-GNSS ground displacement time series (Figure 9b), along with the static GNSS displacement data (Figure 10). The waveform fitting is very comparable to that for the model of Liu et al. (2020), but the inclusion of more recently available hr-GNSS data, which are well fit, adds spatial resolution on the slip. The key advancement of the model is the much improved fit to the DART and tide gauge recordings as shown in Figure 11 compared to that predicted by earlier models (Figures 4 and 5). The amplitudes of the first arrivals are no longer overpredicted and the timing at most DART stations is better than for the starting model in Figure 2b. The prediction of timing and amplitude of long-period arrivals at the DART stations originating from shelf reverberations that leak out into deeper water is comparable or slightly improved by the new model as well, and there is a dramatic reduction of predicted amplitudes of the tide gauge signals in Hawaii (Figure 11b). A 10-min shift of the predicted tsunami signals in Hawaii provides a good match to most of the larger signals and accounts for interference between tsunami waves and background oscillations as well as for neglecting elasticity of the sub-ocean lithosphere and salinity gradients in the water. Shifts of a few minutes can be found for models of tsunami sources along the Aleutian arc (Ye et al., 2022), so the precise shift to apply is not well constrained. Given that there is interference with ambient noise of comparable amplitude at these stations, the most important aspect of the Hawaii tide gauge fits is that the amplitudes are no longer greatly over-predicted. This is a direct result of constraining the slip model entirely beneath the continental shelf to reduce the amount of seafloor uplift beyond the shelf break. Such precise placement of the tsunami excitation influences the offshore wave amplitude from deshoaling of the direct radiated waves as well as the dominant wave periods that have profound effects on the multi-modal oscillations around the Hawaiian Islands (Cheung et al., 2013). The signal at Sand Point is modeled about as well as for the original model. This tide gauge is located in a narrow pass known for strong tidal currents, so we do not expect to match the phase perfectly even with high-resolution bathymetry in our four-level computational grids (Figure 3). The Sand Point signal is comprised of direct and resonant waves over the shallow shelf, which is barely affected by the modification of the seaward edge of the slip model.

The constraint on the final model to have all slip located beneath the shelf is clearly manifested in the peak sea surface elevations predicted for the North Pacific (Figure 12), which can be compared with predictions from Liu et al. (2020) and Ye et al. (2021) (Figure 6). Our final slip model in Figure 7 is spatially intermediate between the models of Liu et al. (2020) and Ye et al. (2021) (Figure 2), and the corresponding far-field tsunami excitation pattern is as well. The results show a similar distribution on the shelf for the model of Liu et al. (2020) (Figure 6d), but with a weaker radiation pattern from reduced uplift beyond the shelf break. Movie S1 shows the evolution of the wave field over the continental margin with time t to elucidate the detailed processes. The rupture lasts for ~90 s with ~80% of the moment release within 1 min. As the initial sea-surface pulse subsides slowly on the shallow shelf, a partial nodal line of reduced wave amplitude becomes evident along the shelf edge by 8 min, indicating energy entrapment on the shelf and leakage onto the slope. Meanwhile radiated waves from the subtle uplift near the shelf edge transform and deshoal over the undulating continental slope before propagating onto the open ocean. The free surface at the source drops to the lowest elevation in ~35 min before bouncing back to its peak at t = 1:10 giving a dominant wave period of ~70 min over the shelf. A distinct oscillation develops over the shoal surrounded by the Shumagin Islands with ~110 min period and a full cycle from t = 1:10 to 3:00. The partial nodal line is still in place with development of shorter-period waves on the shelf and continuing leakage of energy onto the slope. Movie S2 shows superposition of the direct radiated waves on the longer period leaked waves that accounts for the steeper and larger initial arrivals at the DARTs within the first 2 hours. The leakage of long-period energy from the shelf is persistent, resulting in a rather regular concentric wave pattern across the north Pacific. Dispersion of the direct radiated waves leads to a series of shorter period excitations in the range of shelf resonance along the Hawaiian Islands (Cheung et al., 2013).

The final model produced here has good similarity to the main features in the tsunami inversion by Mulia et al. (2022), as shown by comparison of the slip patterns in Figure S2 in Supporting Information S1. The model here fits many more data, including teleseismic body waves, regional broadband and strong motion seismic waves, and hr-GNSS waveforms, along with the GNSS statics and tsunami waveforms used by Mulia et al. (2022). A western slip patch is resolved by those inversions that include seismic data, as noted by Xiao et al. (2021). The

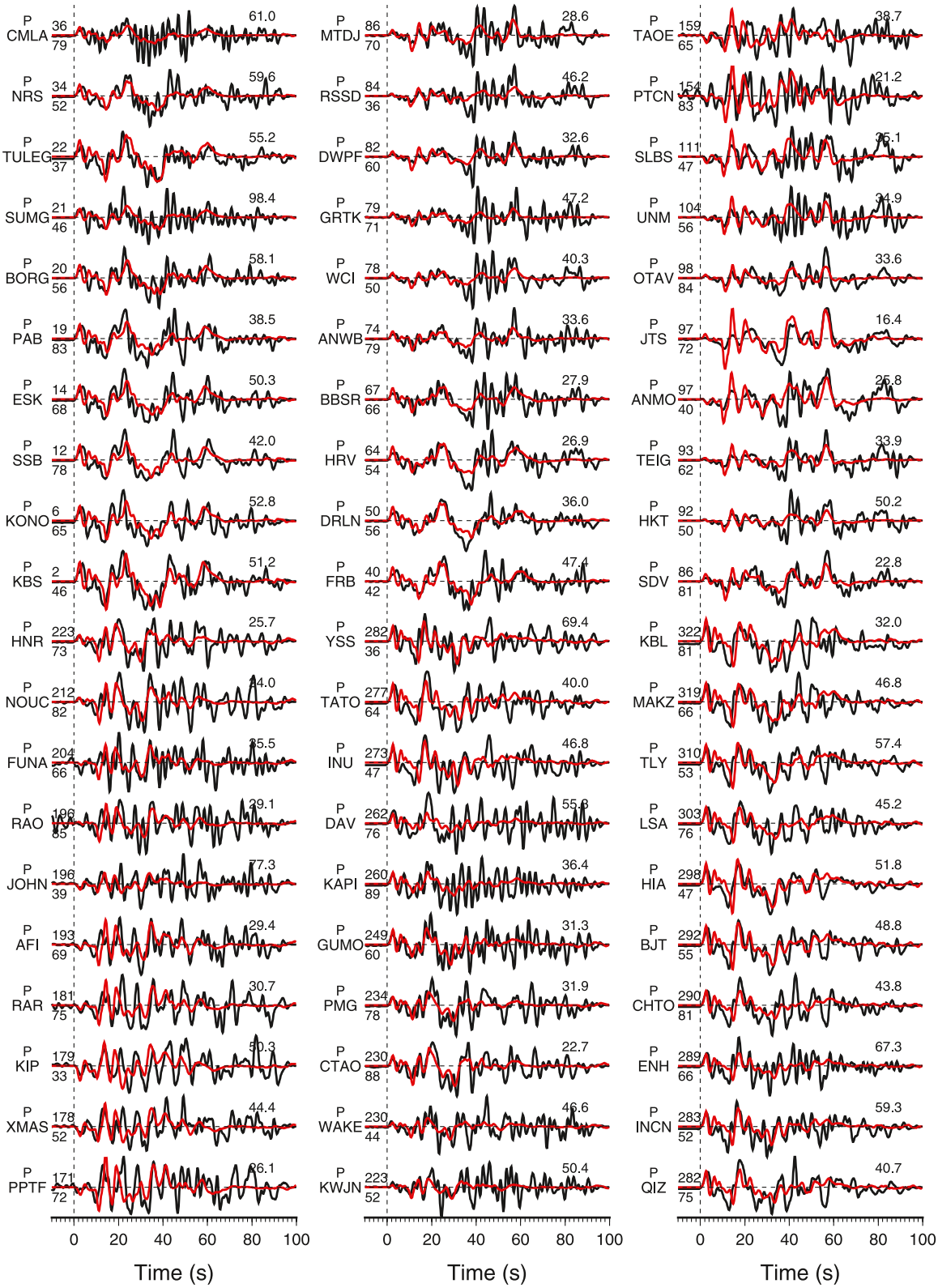

Figure 8. Observed (black) and computed (red) teleseismic *P* and *SH* broadband ground velocity comparisons for the final model from iterative inversion and forward modeling. The phase type and station name, the azimuth (top number, in degrees), and epicentral distance (lower number, in degrees) are shown on the left of each trace comparison. The peak amplitude of the observed traces in microns/s is shown at the top right of each comparison.

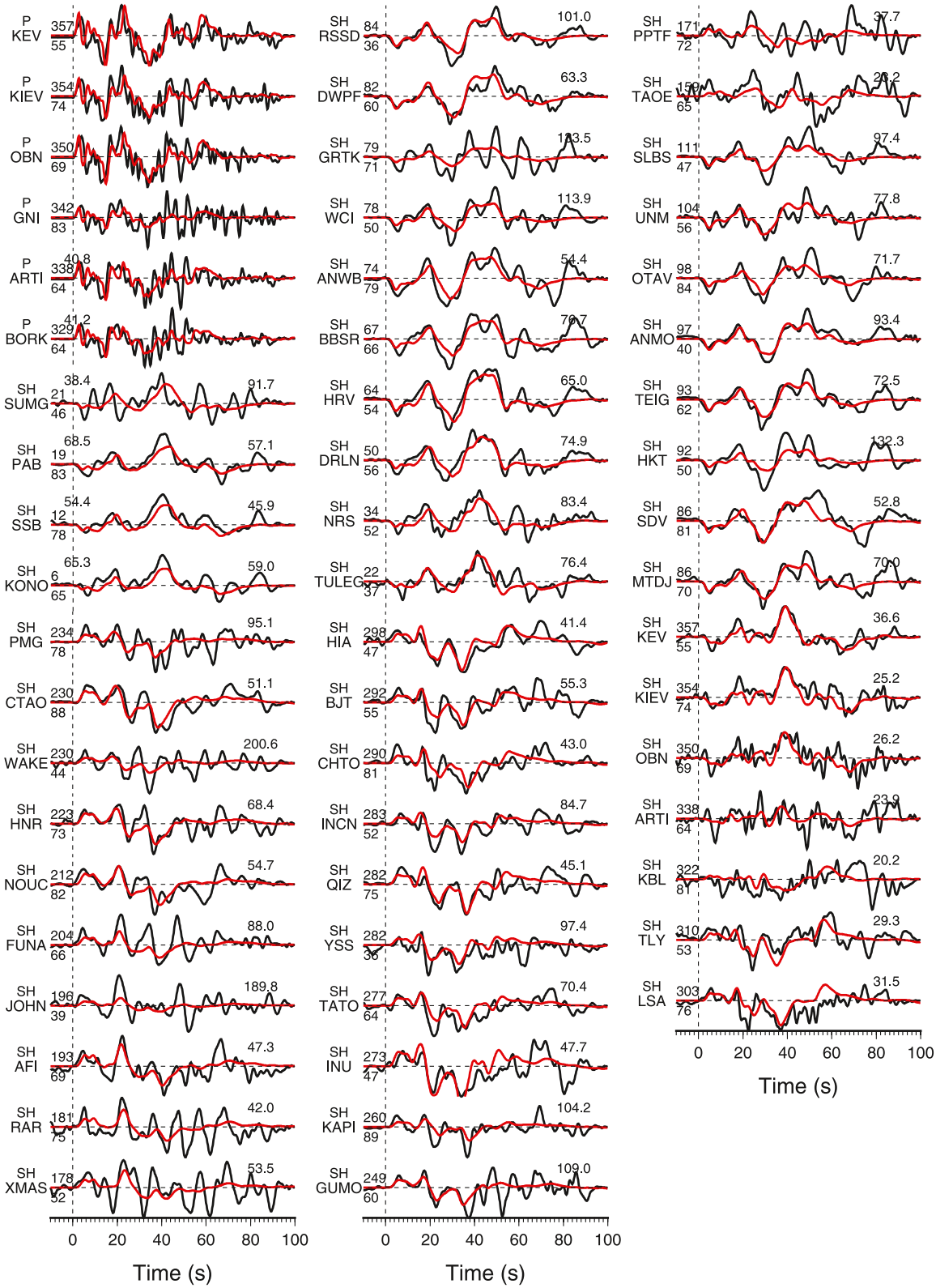

Figure 8. (Continued)

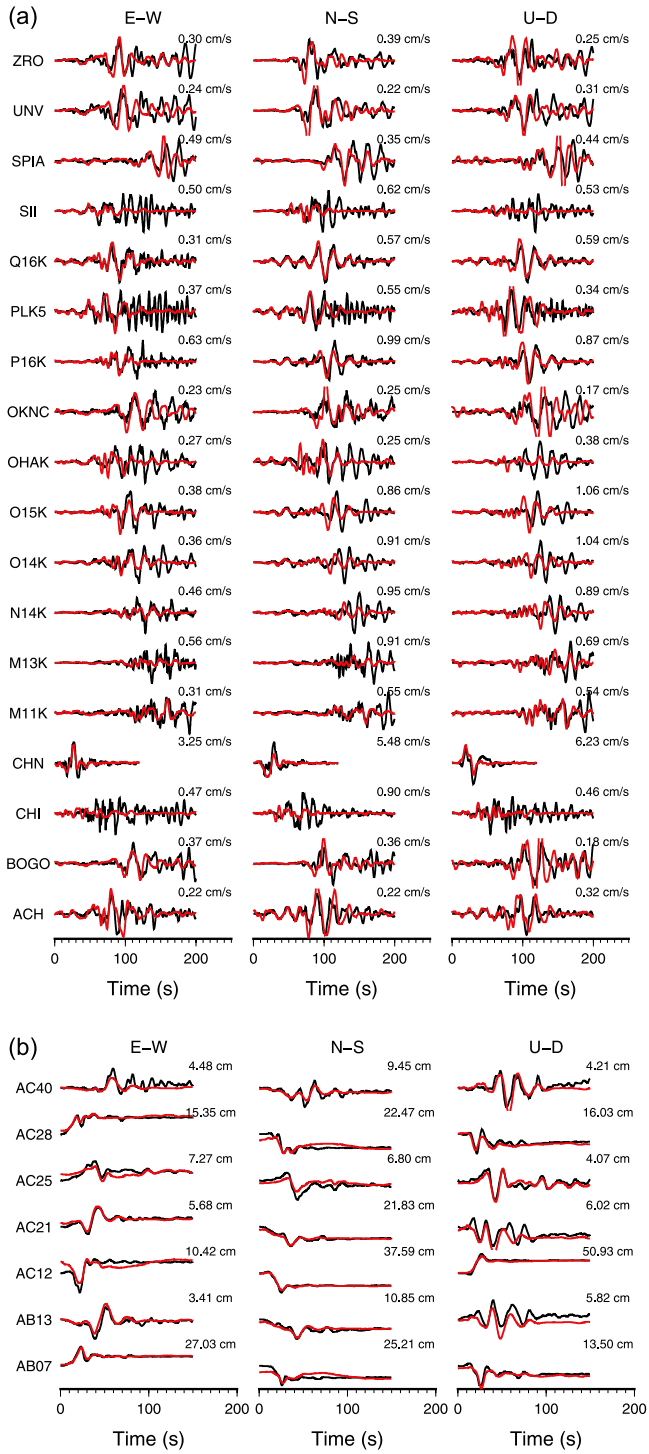

Figure 9. Comparison of observed (black traces) and computed (red traces) (a) three-component broadband regional seismic ground velocities and (b) hr-GNSS displacement waveforms for the final model from iterative inversion and forward modeling.

peak slip in our final model is about 3.5 m. While the down-dip slip extends to ~40 km depth consistent with predictions from most other models, the forward tsunami modeling constrains the up-dip slip limit to 25 km, which is 5 km deeper than the linear inversion prediction of Mulia et al. (2022). The final model here accounts for most available observations, but does not attempt to include the complex InSAR data modeled by Xiao et al. (2021).

5. Discussion

This analysis emphasizes the sensitivity of seaward tsunami excitation to precise placement of slip on the megathrust for earthquakes that rupture beneath shallow continental platforms. This situation effectively traps tsunami energy within a shallow waveguide, with leakage of deshoaled waves into deep water persisting for hours (Figure 11; Movies S1 and S2). When slip extends further up-dip and produces seafloor deformation on the continental slope, there is an abrupt increase in far-field tsunami amplitudes. It is very challenging to resolve the up-dip extent of the slip distribution with seismic and limited geodetic observations alone, particularly if a rapid analysis is needed for a reliable tsunami warning. One strategy would be to incorporate DART observations in the rapid USGS finite-fault inversions (or at least, in forward predictions), particularly those now including geodetic and regional seismic data in the analysis, as was done for the July 29, 2021 Chignik, Alaska M_W 8.2 earthquake (https://earthquake.usgs.gov/earthquakes/eventpage/ak0219neiszm/finite-fault?source=us%26code=ak0219neiszm_2).

The model in Figure 7 has a seismic moment $M_0 = 7.3 \times 10^{20}$ Nm ($M_W = 7.8$). The maximum slip of ~3.5 m, located down-dip of the hypocenter, is comparable to ~3.2 m reported by Liu et al. (2020) and ~3.8 m by Ye et al. (2021). The slip-weighted centroid depth is 35.3 km, similar to the global centroid moment-tensor (GCMT) solution (36.3 km). Usually, large earthquakes are thought to occur in areas with a high slip deficit. However, the peak slip of the 2020 Simeonof event is far less than the potential cumulative slip deficit of ~6 m since the 1917 event (assuming a plate convergence rate of 6 cm/yr). The lower coseismic slip is compatible with the <0.4 geodetic coupling estimate below the Shumagin Islands (Figure 1), which can be interpreted as a patchy locked distribution surrounded by creeping regions. It is plausible that the patchy slip distribution in the down-dip portion of the megathrust may be smoothed, and hence underestimated in the inversion, but represents complete release of the regional slip deficit detected by geodesy. Despite lack of resolution in the shallow coupling region from geodetic observations (Xiao et al., 2021), the geodetic-based slip deficit models propose higher coupling values near the Shumagin trench (Drooff & Freymueller, 2021; S. Li & Freymueller, 2018), and the 2020 Simeonof earthquake should have enhanced the stresses on this shallow region, driving it closer to failure if it is, in fact, locked.

Our final slip distribution and Coulomb stress changes on the interplate thrust surface from the Slab2 model computed for that slip distribution assuming a friction coefficient of 0.4 and a layered structure are shown with aftershock activity within the first 30 days in Figure 13. The early aftershock activity has concentrations up-dip of the coseismic slip zone, down-dip between large slip patches, and southwest of the rupture, with some overlap with the mainshock slip zone (Figure 13a). Some activity plots within areas of increased Coulomb stress in the eastern portion of the rupture, while some activity in the west locates within areas of reduced Coulomb stress and may represent off-boundary faulting with different faulting orientations or local

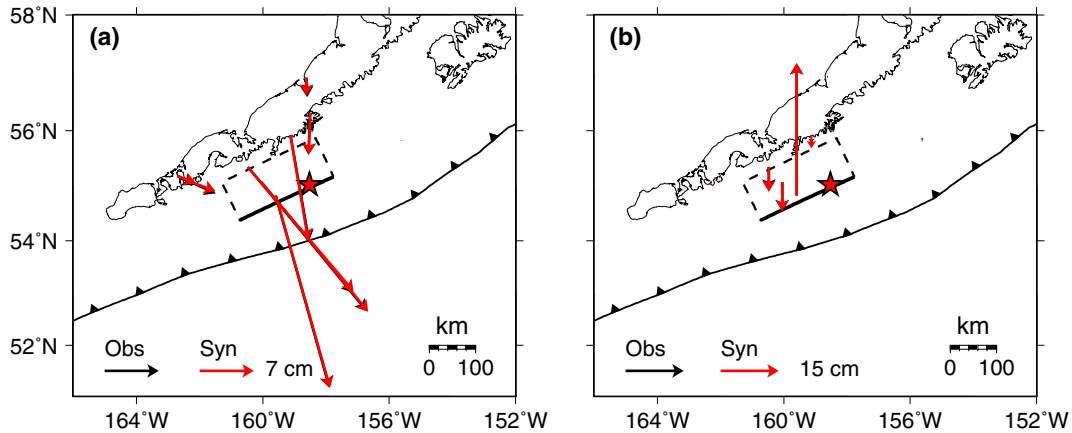

Figure 10. Comparison of observed (black arrows) and computed (red arrows) static displacements at GNSS stations for the final model from iterative inversion and forward modeling. (a) Horizontal displacement. (b) Vertical displacement. The rectangle indicates the assumed fault plane of the final source model with the shallow edge having a solid line. The red star indicates the epicenter.

stress adjustments between the slip patches (Figure 13b). Nineteen out of 20 of the aftershocks with GCMT focal mechanism have shallow-dipping thrust mechanisms (Figure 13b), consistent with our choice of target plane, but the events may be located on or off of the megathrust plane. The aftershocks up-dip of the rupture are largely concentrated in regions with Coulomb stress increases >0.3 MPa, and few events extend toward the trench, where Coulomb stress increases <0.1 MPa occur. The frictional properties of the shallow megathrust are not known, so the increased Coulomb stress may drive release of any accumulated megathrust slip deficit in a shallow earthquake, or alternatively, aseismic afterslip deformation may do so. The model predicts small Coulomb stress reduction in the vicinity of the hypocenter of the 2021 Chignik earthquake, but this is controlled by minor slip at the northeast end of the 2020 rupture that is not well-resolved. Coulomb stress increase is predicted across the 2021 rupture zone further to the northeast.

The mainshock rupture area was limited between 25 and 40 km depth with three main slip patches, which did not extend to the shallow part of the megathrust, exhibiting an abrupt edge to coseismic slip along the up-dip margin. Geometric barriers can cause abrupt rupture truncations; seismic reflection profiles indicate a heterogeneous shallow structure seaward of the shelf break along the Shumagin gap (Bécel et al., 2017; Shillington et al., 2022), and this may constitute an obstacle to rupture extending shallower. A comparison of two reflection profiles transecting the Shumagin gap with the preferred model from this paper is shown in Figure 14. The depth of the plate boundary used for the model and the Slab2 interface are compatible with the reflection interface. It is notable that the region with large slip at depth >25 km has a several kilometer thick zone of reflections, distinct from the narrow zone of reflections in the up-dip portion of the megathrust without coseismic slip. Splay faults in the overriding plate may also act as barriers to rupture propagation along the megathrust to the trench (e.g., Collot et al., 2004; Von Huene et al., 2021). In addition, anelastic deformation in any poroelastic material of the sedimentary toe can also effectively prevent earthquake rupture from reaching to the trench (Ma, 2012). Thus, changes in fault geometry or heterogeneities of pore pressure along the shallow sedimentary wedge interface may be significant in controlling the extent of shallow rupture along the Shumagin gap.

6. Conclusions

The 2020 M_W 7.8 Simeonof earthquake is an important event because it is the largest to strike within the Shumagin seismic gap since 1917, confirming that moderate slip deficit accumulation had occurred directly below the Shumagin Islands. Resolving the spatial extent of coseismic slip is crucial to understanding the megathrust properties and strain accumulation in the Shumagin segment, with the up-dip extent of coseismic slip in the mainshock being of particular importance for tsunami hazard assessment in the region and in the far-field. While high-quality finite-fault inversions of seismic and geodetic data sets establish the first-order characteristics of the slip distribution, with most slip located beneath the Shumagin Islands, the models differ by 20 km or more in

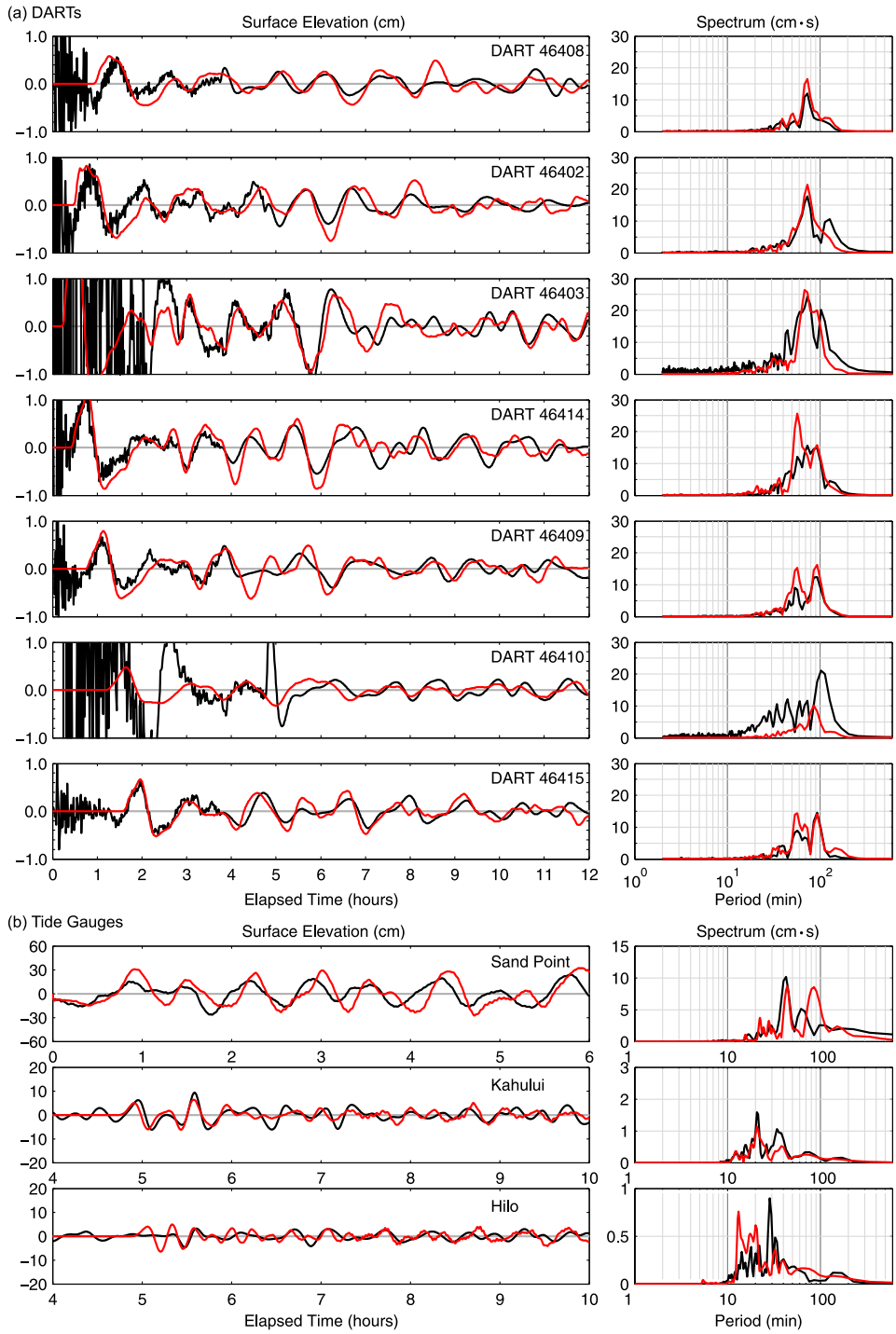

Figure 11. Tsunami predictions at (a) DARTs and (b) tide gauges for the final model from iterative inversion and forward modeling. Observed, de-tided, and lightly low-pass filtered sea surface elevations are shown in black; predicted tsunami signals are shown in red. Time series and amplitude spectra are shown in the left and right columns in each part. The DART time series include high frequency signals generated by passage of seismic waves; these are not included in the model calculations for the tsunami. Time shifts of 10 min have been applied to the Hawaii predictions to adjust for neglected high-order propagation effects in the tsunami calculations and interference from background oscillations in the observations.

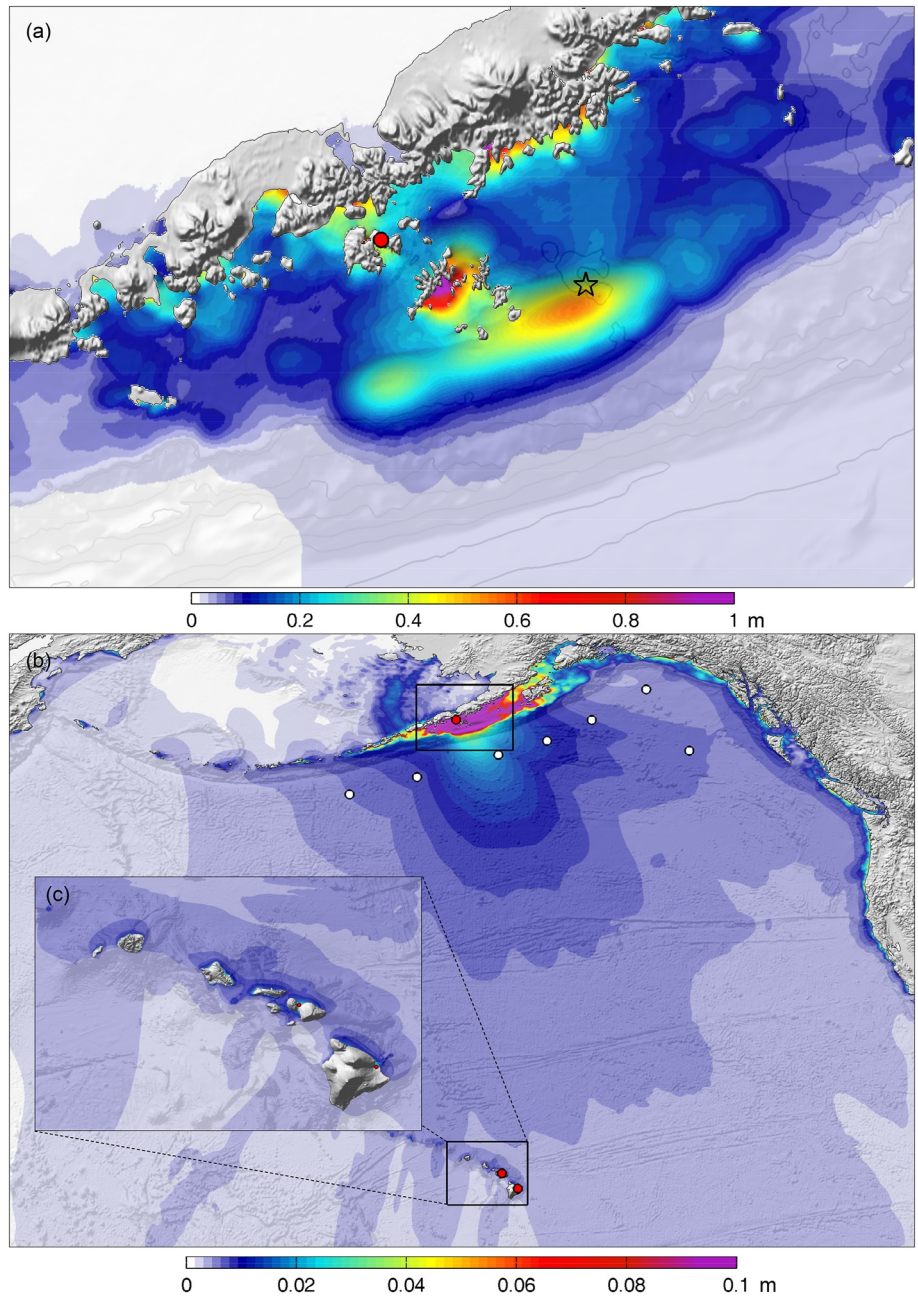

Figure 12. Maximum sea surface elevation map extending from the source region across the northern Pacific to Hawaii predicted for the final model from iterative inversion and forward modeling. (a) Along the Aleutians. (b) Across the Pacific. (c) Around Hawaii. The black open star denotes the epicenter. Red circles indicate the tide gauges and white circles denote the DART stations.

the along-dip placement of slip depending on the data used and the model parameterization. This uncertainty in absolute placement of the slip on the megathrust is particularly important for rupture that occurs under the continental shelf versus under the continental slope due to the effects on the resulting tsunami.

Published models give tsunami predictions that straddle seaward observations, prompting an iterative refinement in seeking a self-consistent rupture model that accounts for seismic, geodetic, and tsunami observations. The pronounced senstivity to slip placement and resulting seafloor uplift in proximity to the shelf break is exploited to perturb the models to achieve good fits to all data, with all slip constrained to beneath the shelf and only minor uplift extending beyond the shelf break. This constraint on the up-dip edge of coseismic rupture is particularly

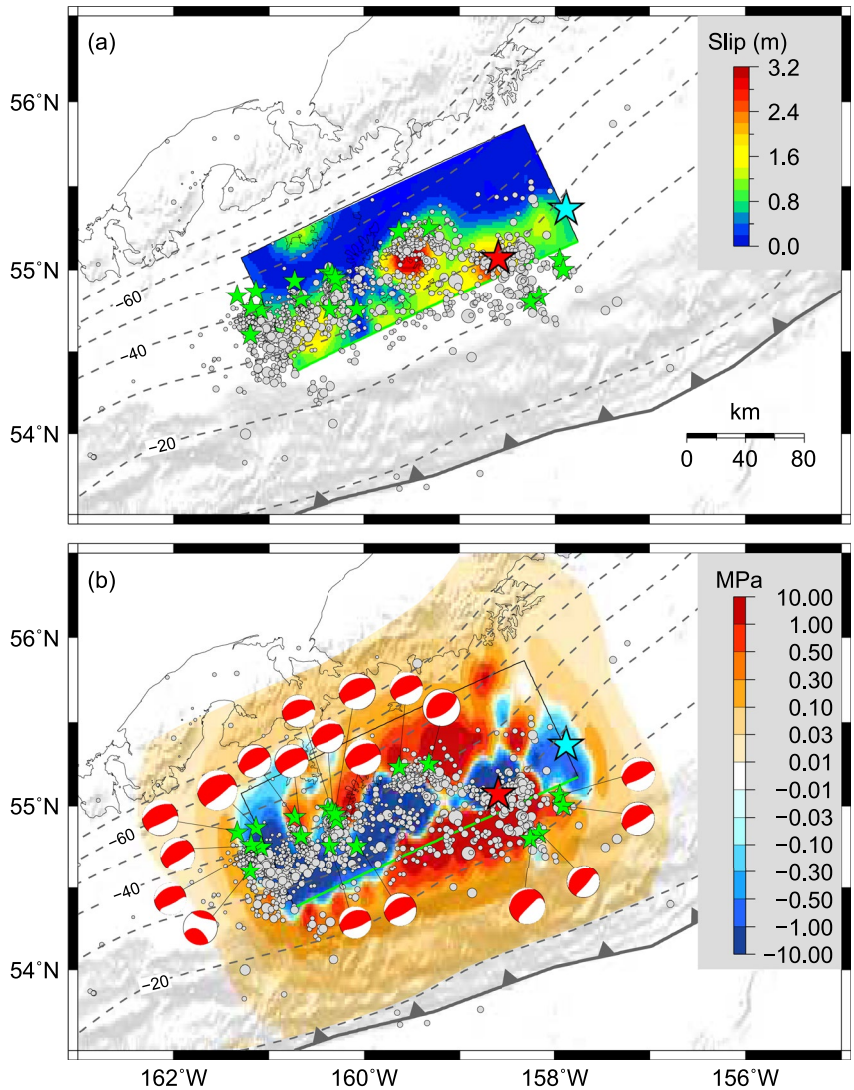

Figure 13. (a) Superposition of U.S. Geological Survey National Earthquake Information Center (USGS-NEIC) aftershocks with magnitude ≥2.5 on the preferred slip model for the first month after the 22 July 2020 Simeonof earthquake, with the circle sizes scaled by magnitude. The red star indicates the epicenter of the 2020 mainshock, and the cyan star shows the epicenter of the 29 July 2021 M_W 8.2 Chignik earthquake.The depth contours of the slab interface model, Slab2, are shown by dashed lines, labeled in km. The green stars represent the first month of aftershocks with magnitudes ≥5.0. (b) Computed Coulomb stress changes for thrust faulting on the Slab2 plate interface for the final slip model. The black rectangle indicates the assumed fault plane of the final slip model, with the shallow edge having a green line. Global centroid moment-tensor (GCMT) focal mechanisms with magnitudes ≥5.0 for the first month are shown in red.

significant for Hawaii, for which a factor of about 5 difference in tsunami amplitude results from minor shifts (~20 km) of the source models along dip. Aftershocks up-dip of the rupture zone extend to below the shelf break, in regions where the increment of Coulomb stress exceeded 0.3 MPa, but only a handful of aftershocks locate beneath the continental slope where smaller Coulomb stress increases were produced. The shallow megathrust below the slope may undergo afterslip releasing accumulated strain, but the possibility of a large tsunami earthquake in this region has not been ruled out.

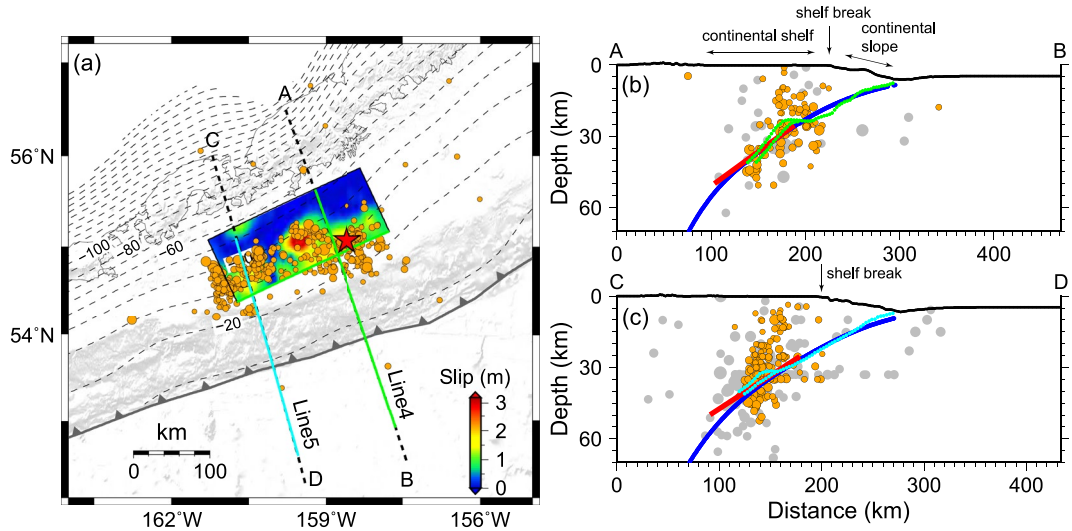

Figure 14. Comparison of the final fault model geometry and slip distribution, background activity (gray dots), and aftershocks (gold dots) with reflection profiles along ALEUT Line 4 and Line 5 from Bécel et al. (2017) and Shillington et al. (2022) in map view (left) and in cross-section (right). The red star in (a) indicates the 2020 epicenter. The dashed contours in (a) and the blue curves in (b) and (c) indicate the plate interface depths from Slab2. The regions of the continental shelf at water depths less than 200 m, the shelf break at 200 m depth, and the continental slope are indicated. The red lines in (b) and (c) indicate projection of the fault model. The light green and cyan curves in (b) and (c) indicate the plate interface reflection zone for Line 4 and Line 5, respectively. The thick zones of high reflectivity at depths greater than 25–35 km in Line 4 and Line 5 indicate regions with multiple reflections, interpreted as subducted sediment layer.

Acknowledgments
We thank Jeff Freymueller and an anonymous reviewer for helpful reviews of the manuscript as well as the editor Rachel Abercrombie and the assigned associated editor forthoughtful comments and careful proofreading. Yoshiki Yamazaki provided the initial tsunami model set up from an earlier study. The GNSS data is based on services provided by the GAGE Facility, operated by UNAVCO, Inc., with support from the National Science Foundation and the National Aeronautics and Space Administration under NSF Cooperative Agreement EAR1724794. We thank the facilities of IRIS Data Services, and specifically the IRIS Data Management Center, which were used for access to waveforms, related metadata, and/or derived products used in this study. IRIS Data Services are funded through the Seismological Facilities for the Advancement of Geoscience (SAGE) Award of the National Science Foundation under Cooperative Support Agreement EAR1851048. We also thank the CSRS-PPP online service system for hr-GNSS data processing (https://webapp.geod.nrcan.gc.ca/geod/tools-outils/ppp.php). Yefei Bai's tsunami research is supported by Finance Science and Technology Project of Hainan Province (No. ZDKJ202019). C. Liu was supported by the National Science Foundation of China (No. 41974056). Thorne Lay's earthquake research is supported by National Science Foundation (Grant EAR1802364). Lingling Ye's earthquake study is supported by National Natural Science Foundation of China (No. 41874056).

Data Availability Statement

Co-seismic GNSS displacements and hr-GNSS time series were obtained from the UNAVCO Bulletin Board (https://www.unavco.org/event-response/july-28-2021-m-8-2-alaska-earthquake/). Teleseismic body wave and regional broadband records were obtained from the Federation of Digital Seismic Networks (FDSN: https://doi.org/10.7914/SN/IU, https://doi.org/10.7914/SN/II, https://doi.org/10.7914/SN/CN, https://doi.org/10.18715/GEOSCOPE.G, https://doi.org/10.7914/SN/CU, https://doi.org/10.7914/SN/IC, https://doi.org/10.7914/SN/AV, https://doi.org/10.7914/SN/AK, https://doi.org/10.7914/SN/TA), and accessed through the Incorporated Research Institutions for Seismology (IRIS) data management center (http://ds.iris.edu/wilber3/find_event). Strong-motion recordings were obtained from the Center for Engineering Strong Motion Data (CESMD, https://strongmotion-center.org/). Earthquake information is based on the catalogs from the U.S. Geological Survey National Earthquake Information Center (USGS-NEIC) (https://earthquake.usgs.gov/earthquakes) and the Alaska Earthquake Center (http://earthquake.alaska.edu), last accessed November 16, 2021. The high-resolution digital elevation model, Sand Point V2, at the Shumagin Islands was downloaded from the National Centers for Environmental Information (https://maps.ngdc.noaa.gov/viewers/bathymetry/).

References

Azouri, A. (2016). *Observations, forecast, and modeling of 0.5–200 min infragravity oscillations in Haleiwa Harbor region, Hawaii*. PhD Dissertation. Honolulu: University of Hawaii.

Bai, Y., Cheung, K. F., Yamazaki, Y., Lay, T., & Ye, L. (2014). Tsunami surges around the Hawaiian islands from the 1 April 2014 North Chile M_W 8.1 earthquake. *Geophysical Research Letters*, *41*, 8512–8521. https://doi.org/10.1002/2014gl061686

Bai, Y., Yamazaki, Y., & Cheung, K. F. (2015). Interconnection of multi-scale standing waves across the Pacific from the 2011 Tohoku tsunami. *Ocean Modelling*, *92*, 183–197. https://doi.org/10.1016/j.ocemod.2015.06.007

Bécel, A., Shillington, D. J., Delescluse, M., Nedimović, M. R., Abers, G. A., Saffer, D. M., et al. (2017). Tsunamigenic structures in a creeping section of the Alaska subduction zone. *Nature Geoscience*, *10*(8), 609–613.

Boyd, T. M., & Lerner-Lam, A. L. (1988). Spatial distribution of turn-of-the-century seismicity along the Alaska-Aleutian arc. *Bulletin of the Seismological Society of America*, *78*, 636–650.

Boyd, T. M., Taber, J. J., Lerner-Lam, A. L., & Beavan, J. (1988). Seismic rupture and arc segmentation within the Shumagin Islands seismic gap, Alaska. *Geophysical Research Letters*, *15*, 201–204. https://doi.org/10.1029/gl015i003p00201

Briggs, R. W., Engelhart, S. E., Nelson, A. R., Dura, T., Kemp, A. C., Haeussler, P. J., et al. (2014). Uplift and subsidence reveal a nonpersistent megathrust rupture boundary (Sitkinak Island, Alaska). *Geophysical Research Letters*, *41*, 2289–2296. https://doi.org/10.1002/2014gl059380

Cheung, K. F., Bai, Y., & Yamazaki, Y. (2013). Surges around the Hawaiian islands from the 2011 Tohoku tsunami. *Journal of Geophysical Research*, *118*(10), 5703–5719. https://doi.org/10.1002/jgrc.20413

Collot, J.-Y., Marcaillou, B., Sage, F., Michaud, F., Agudelo, W., Charvis, P., et al. (2004). Are rupture zone limits of great subduction earthquakes controlled by upper plate structures? Evidence from multichannel seismic reflection data acquired across the northern Ecuador—Southwest Colombia margin. *Journal of Geophysical Research*, *109*, B11103. https://doi.org/10.1029/2004jb003060

Crowell, B. W., & Melgar, D. (2020). Slipping the Shumagin gap: A kinematic coseismic and early afterslip model of the M_w 7.8 Simeonof Island, Alaska, earthquake. *Geophysical Research Letters*, *113*, e2020GL090308.

Davies, J., Sykes, L., House, L., & Jacob, K. (1981). Shumagin seismic gap, Alaska Peninsula: History of great earthquakes, tectonic setting, and evidence for high seismic potential. *Journal of Geophysical Research*, *86*, 3821–3855. https://doi.org/10.1029/jb086ib05p03821

DeMets, C., Gordon, R. G., & Argus, D. F. (2010). Geologically current plate motions. *Geophysical Journal International*, *181*, 1–80. https://doi.org/10.1111/j.1365-246x.2009.04491.x

Drooff, C., & Freymueller, J. T. (2021). New constraints on slip deficit on the Aleutian megathrust and inflation at Mt. Veniaminof, Alaska from repeat GPS measurements. *Geophysical Research Letters*, *48*, e2020GL091787. https://doi.org/10.1029/2020gl091787

Estabrook, C. H., & Boyd, T. M. (1992). The Shumagin Islands, Alaska, earthquake of 31 May 1917. *Bulletin of the Seismological Society of America*, *82*, 755–773.

Freymueller, J. T., & Beavan, J. (1999). Absence of strain accumulation in the western Shumagin segment of the Alaska subduction zone. *Geophysical Research Letters*, *26*, 3233–3236. https://doi.org/10.1029/1999gl008356

Hayes, G. P., Moore, G. L., Portner, D. E., Hearne, M., Flamme, H., Furtney, M., & Smoczyk, G. M. (2018). Slab2, a comprehensive subduction zone geometry model. *Science*, *362*(6410), 58–61. https://doi.org/10.1126/science.aat4723

Heidarzadeh, M., Murotani, S., Satake, K., Ishibe, T., & Gusman, A. R. (2016). Source model of the 16 September 2015 Illapel, Chile, M_w 8.4 earthquake based on teleseismic and tsunami data. *Geophysical Research Letters*, *43*, 643–650. https://doi.org/10.1002/2015gl067297

Ji, C., Helmberger, D. V., Wald, D. J., & Ma, K. F. (2003). Slip history and dynamic implications of the 1999 Chi-Chi, Taiwan, earthquake. *Journal of Geophysical Research: Solid Earth*, *108*(B9). https://doi.org/10.1029/2002jb001764

Ji, C., Wald, D. J., & Helmberger, D. V. (2002). Source description of the 1999 Hector Mine, California, earthquake, part I: Wavelet domain inversion theory and resolution analysis. *Bulletin of the Seismological Society of America*, *92*(4), 1192–1207. https://doi.org/10.1785/0120000916

Larson, K. M., Lay, T., Yamazaki, Y., Cheung, K. F., Ye, L., Williams, S. D. P., & Davis, J. L. (2021). Dynamic sea level variation from GNSS: 2020 Shumagin earthquake tsunami resonance and Hurricane Laura. *Geophysical Research Letters*, *48*, e2020GL091378. https://doi.org/10.1029/2020gl091378

Lay, T. (2018). A review of the rupture characteristics of the 2011 Tohoku-oki M_w 9.1 earthquake. *Tectonophys*, *733*, 4–36. https://doi.org/10.1016/j.tecto.2017.09.022

Li, L., & Cheung, K. F. (2019). Numerical dispersion in non-hydrostatic modeling of long-wave propagation. *Ocean Modelling*, *138*, 68–87. https://doi.org/10.1016/j.ocemod.2019.05.002

Li, L., Lay, T., Cheung, K. F., & Ye, L. (2016). Joint modeling of teleseismic and tsunami wave observations to constrain the 16 September 2015 Illapel, Chile, M_w 8.3 earthquake rupture process. *Geophysical Research Letters*, *43*, 4303–4312. https://doi.org/10.1002/2016gl068674

Li, S., & Freymueller, J. T. (2018). Spatial variation of slip behavior beneath the Alaska Peninsula along Alaska-Aleutians subduction zone. *Geophysical Research Letters*, *45*, 3453–3460. https://doi.org/10.1002/2017gl076761

Liu, C., Lay, T., Xiong, X., & Wen, Y. (2020). Rupture of the 2020 M_w 7.8 earthquake in the Shumagin gap inferred from seismic and geodetic observations. *Geophysical Research Letters*, *47*, e2020GL090806. https://doi.org/10.1029/2020gl090806

Ma, S. (2012). A self-consistent mechanism for slow dynamic deformation and tsunami generation for earthquakes in the shallow subduction zone. *Geophysical Research Letters*, *39*(11), L11310. https://doi.org/10.1029/2012gl051854

Mulia, I. E., Heidarzadeh, M., & Satake, K. (2022). Effects of depth of fault slip and continental shelf geometry on the generation of anomalously long-period tsunami by the July 2020 *M*w 7.8 Shumagin (Alaska) earthquake. *Geophysical Research Letters*, *49*, e2021GL094937.

Okada, Y. (1985). Surface deformation due to shear and tensile faults in a half-space. *Bulletin of the Seismological Society of America*, *75*, 1135–1154. https://doi.org/10.1785/BSSA0750041135

Shillington, D. J., Bécel, A., & Nedimovic, M. R. (2022). Upper plate structure and megathrust properties in the Shumagin gap near the July 2020 M7.8 Simeono event. *Geophysical Research Letters*, *49*, 32021GL096974. https://doi.org/10.1029/2021gl096974

Sykes, L. R., Kissinger, J. B., House, L., Davies, J. N., & Jakob, K. H. (1981). Rupture zones of great earthquakes in the Alaska-Aleutian Arc, 1784 – 1980. In D. W. Simpson, & P. G. Richards (Eds.), *Earthquake prediction – An international review* (pp. 73–80). Maurice Ewing series 4. Washington, D.C.: American Geophysical Union.

Tanioka, Y., & Satake, K. (1996). Tsunami generation by horizontal displacement of ocean bottom. *Geophysical Research Letters*, *23*, 861–864. https://doi.org/10.1029/96gl00736

U.S.G.S. (2013). Alaska earthquake source for the SAFRR tsunami scenario. Open-File Report 2013-1170-B, California Geological Survey Special Report 229.

Von Huene, R., Miller, J. J., & Krabbenhoeft, A. (2021). The Alaska convergent margin backstop splay fault zone, a potential large tsunami generator between the frontal prism and continental framework. *Geochemistry, Geophysics, Geosystems*, *22*, e2019GC008901. https://doi.org/10.1029/2019gc008901

Witter, R. C., Briggs, R. W., Engelhart, S. E., Gelfenbaum, G., Koehler, R. D., & Barnhart, W. D. (2014). Little late Holocen strain accumulation and release on the Aleutian megathrust below the Shumagin Islands, Alaska. *Geophysical Research Letters*, *42*, 2359–2367. https://doi.org/10.1002/2014gl059393

Xiao, Z., Freymueller, J. T., Grapenthin, R., Elliott, J. L., Drooff, C., & Fusso, L. (2021). The deep Shumagin gap filled: Kinematic rupture model and slip budget analysis of the 2020 Mw 7.8 Simeonof earthquake constrained by GNSS, global seismic waveforms, and floating InSAR. *Earth and Planetary Science Letters*, *576*, 117241. https://doi.org/10.1016/j.epsl.2021.117241

Yamazaki, Y., Cheung, K. F., & Kowalik, Z. (2011). Depth-integrated, non-hydrostatic model with grid nesting for tsunami generation, propagation, and run-up. *International Journal for Numerical Methods in Fluids*, *67*(12), 2081–2107. https://doi.org/10.1002/fld.2485

Yamazaki, Y., Cheung, K. F., & Lay, T. (2013). Modeling of the 2011 Tohoku near-field tsunami from finite-fault inversion of seismic waves. *Bulletin of the Seismological Society of America*, *103*, 1444–1455. https://doi.org/10.1785/0120120103

Yamazaki, Y., Kowalik, Z., & Cheung, K. F. (2009). Depth-integrated, non-hydrostatic model for wave breaking and run-up. *International Journal for Numerical Methods in Fluids*, *61*(5), 473–497. https://doi.org/10.1002/fld.1952

Yamazaki, Y., Lay, T., Cheung, K. F., Yue, H., & Kanamori, H. (2011). Modeling near-field tsunami observations to improve finite-fault slip models for the 11 March 2011 Tohoku earthquake. *Geophysical Research Letters*, *38*(7), L00G15. https://doi.org/10.1029/2011gl049130

Ye, L., Bai, Y., Si, D., Lay, T., Cheung, K.F., & Kanamori, H. (2022). Rupture Model for the 29 July 2021 Mw 8.2 Chignik, Alaska Earthquake Constrained by Seismic, Geodetic, and Tsunami Observations. *Journal of Geophysical Research: Solid Earth*, *127*, e2021JB023676. https://doi.org/10.1029/2021JB023676

Ye, L., Kanamori, H., Avouac, J. P., Li, L., Cheung, K. F., & Lay, T. (2016). The 16 April 2016, M_W 7.8 (M_S 7.5) Ecuador earthquake: A quasi-repeat of the 1942 M_S 7.5 earthquake and partial re-rupture of the 1906 M_S 8.6 Colombia–Ecuador earthquake. *Earth and Planetary Science Letters*, *454*, 248–258.

Ye, L., Lay, T., Kanamori, H., Yamazaki, Y., & Cheung, K. F. (2021). The 22 July 2020 M_W 7.8 Shumagin seismic gap earthquake: Partial rupture of a weakly coupled megathrust. *Earth and Planetary Science Letters*, *562*, 116879. https://doi.org/10.1016/j.epsl.2021.116879

Yue, H., Lay, T., Rivera, L., Bai, Y., Yamazaki, Y., Cheung, K. F., et al. (2014). Rupture process of the 2010 M_W 7.8 Mentawai tsunami earthquake from joint inversion of near-field hr-GPS and teleseismic body wave recordings constrained by tsunami observations. *Journal of Geophysical Research: Solid Earth*, *119*, 5574–5593. https://doi.org/10.1002/2014jb011082

Journal of Geophysical Research: Solid Earth

Supporting Information for

Optimizing a model of coseismic rupture for the 22 July 2020 Mw 7.8 Shumagin earthquake by exploiting acute sensitivity of tsunami excitation across the shelf break

Yefei Bai[1,2], Chengli Liu[3], Thorne Lay[4], Kwok Fai Cheung[5], Lingling Ye[6]

[1] Ocean College, Zhejiang University, Zhoushan, Zhejiang, 316021, China

[2] Hainan Institute, Zhejiang University, Sanya, Hainan, 572024, China

[3] Institute of Geophysics and Geomatics, China University of Geosciences, Wuhan, Hubei, 43007，China

[4] Department of Earth and Planetary Sciences, University of California Santa Cruz, Santa Cruz, CA 95064, USA

[5] Department of Ocean and Resources Engineering, University of Hawaii at Manoa, Honolulu, HI, 96822, USA

[6] Department of Earth and Space Sciences, Southern University of Science and Technology, Shenzhen, 518055, China

Corresponding author: Yefei Bai (yfbai@zju.edu.cn)

Contents of this file

Figure S1 and S2
Movies S1 and S2

Introduction

This supporting information provides two additional figures and captions for 2 video animations (separately submitted) to support the discussions in the main text.

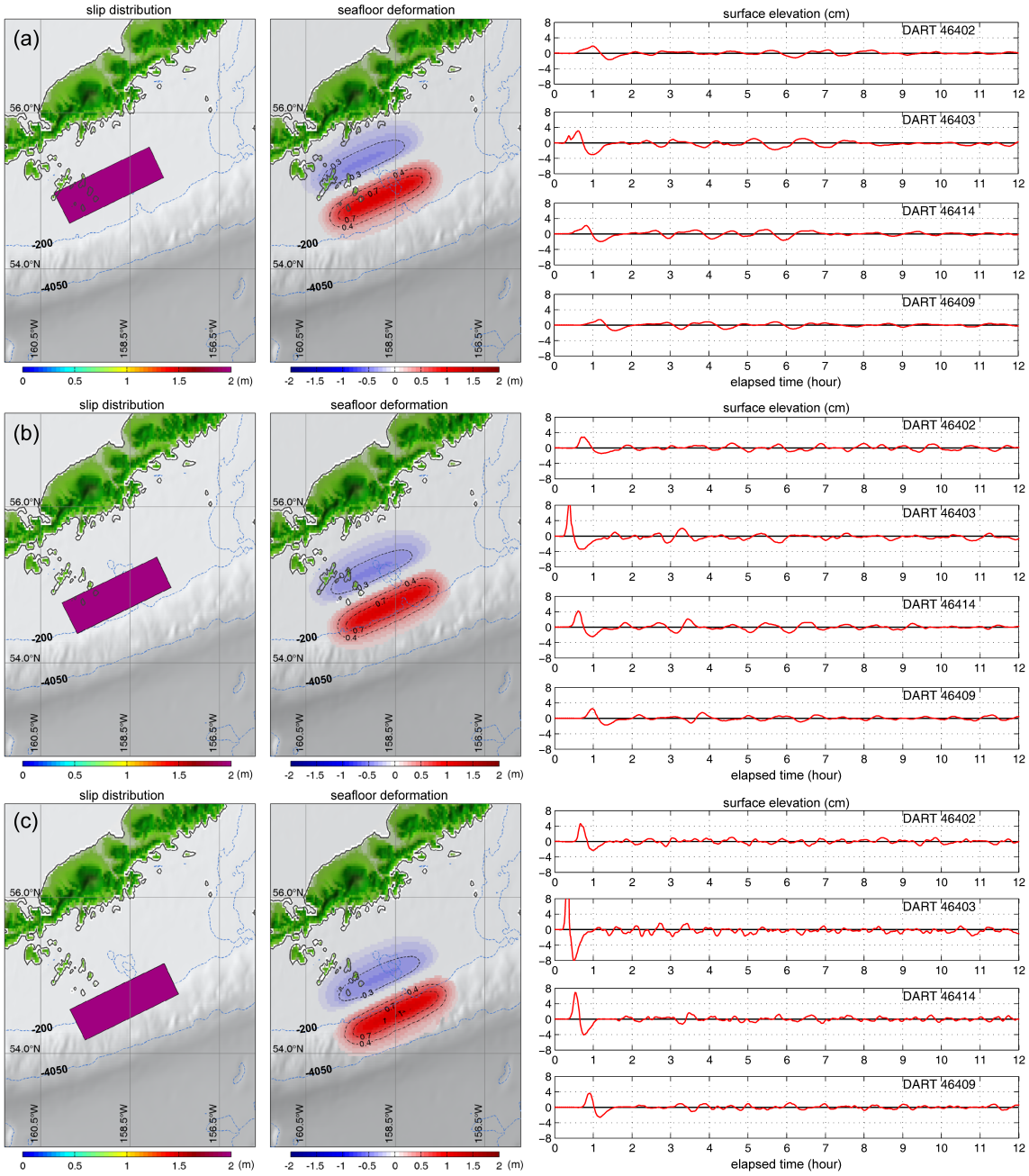

Figure S1. Demonstration of the acute sensitivity of seaward tsunami radiation to the placement of slip relative the continental shelf and continental slope (extending from the northern 200 m depth blue dashed line to the trench). Uniform slip models scaled to match the seismic moment of the 2020 Shumagin earthquake (7.3 x 10^{20} Nm) are shown in the left column, the corresponding vertical deformation of the seafloor in the middle column, and computed tsunami signals at the nearest four DART stations (see Figure 3 for locations) on a common amplitude scale in the right column. Note that when slip and seafloor motion is located entirely beneath the shelf, as in (a), the tsunamis at DART stations have low amplitude, long-period arrivals. As slip approaches the shelf break and produces some uplift of the continental slope as in (b), the tsunamis have shorter periods and larger amplitudes. When slip extends partly under the continental slope producing large uplift of the continental slope, the tsunami amplitudes are large and shorter period waves are excited.

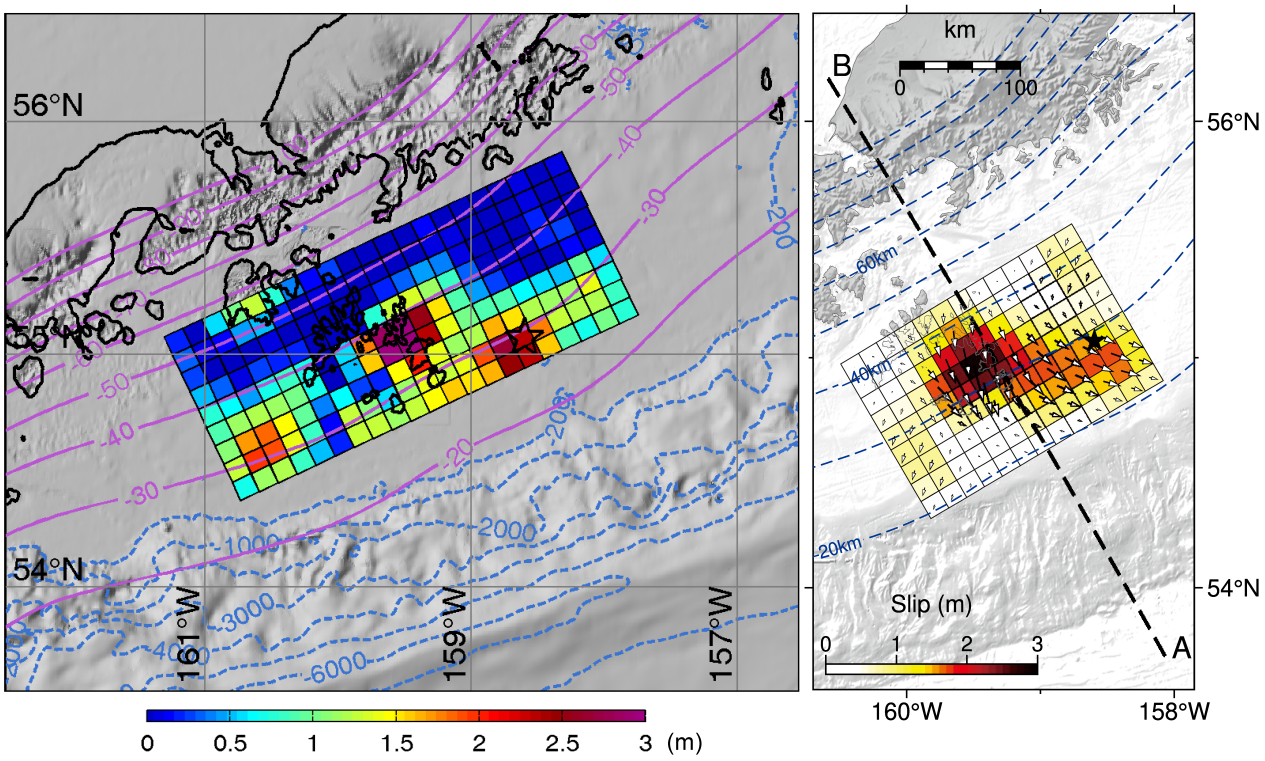

Figure S2. Comparison of (left) the final slip model from this study with (right) the tsunami-GNSS statics inversion model of Mulia et al. (2022). The black star denotes the hypocenter. The purple contour in the left panel and the blue dashed contour in the right panel indicate plate interface depths from the Slab2 model. The final model here fits far more data, including teleseismic, regional broadband and strong motion, and hr-GNSS observations, along with the GNSS statics and tsunami waveforms used by Mulia et al. (2022).

Movie S1. Animation of the sea surface elevation produced by the final model in Figure 7. Snapshots from the animation showing resonances along the continental shelf are provided below.

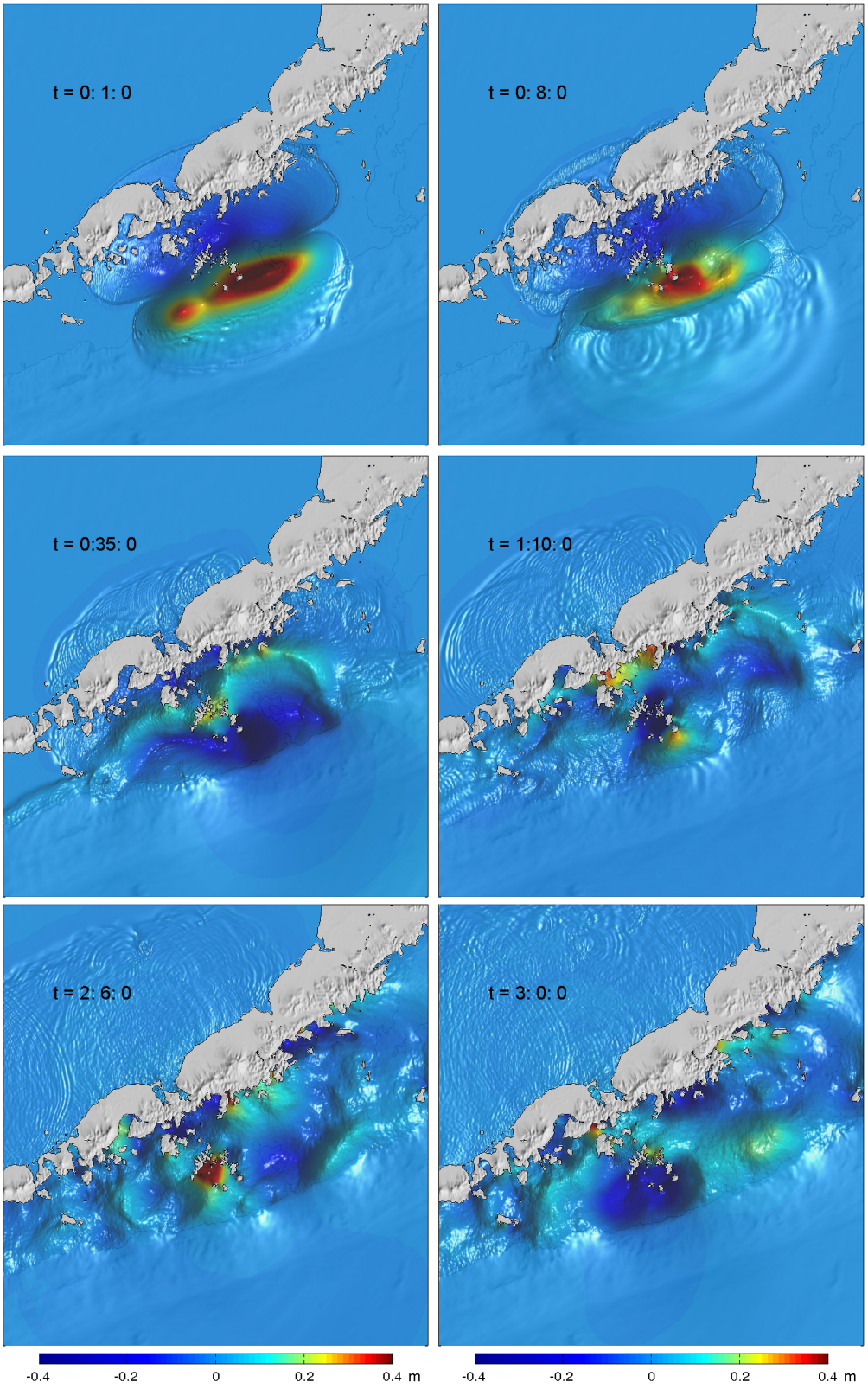

Movie S2. Animation of the far-field sea surface elevation produced by the final model in Figure 7. Snapshots from the animation showing superposition of short-period direct radiated and long-period leaked waves are provided below.